A novel machine learning model to predict the moment capacity of cold-formed steel channel beams with edge-stiffened and un-stiffened web holes

Article *in* Journal of Building Engineering · December 2022

DOI: 10.1016/j.jobe.2022.104592

CITATIONS
61

READS
626

6 authors, including:

Yecheng Dai
University of Auckland
20 PUBLICATIONS **323** CITATIONS
SEE PROFILE

Krishanu Roy
University of Auckland
195 PUBLICATIONS **4,667** CITATIONS
SEE PROFILE

Zhiyuan Fang
University of Waikato
66 PUBLICATIONS **1,347** CITATIONS
SEE PROFILE

Boshan Chen
Hainan University
69 PUBLICATIONS **1,423** CITATIONS
SEE PROFILE

A novel machine learning model to predict the moment capacity of cold-formed steel channel beams with edge-stiffened and un-stiffened web holes

Yecheng Dai[a], Krishanu Roy[b*], Zhiyuan Fang[a], Boshan Chen[c], Gary M. Raftery[a], James B.P. Lim[a, b]

a Department of Civil and Environmental Engineering, The University of Auckland, New Zealand

b School of Engineering, The University of Waikato, New Zealand

c Department of Civil Engineering, Tsinghua University, China

*Corresponding Author Contact Details: Krishanu Roy

E: kroy405@aucklanduni.ac.nz, The University of Waikato, Hamilton 3216, New Zealand, T: +64 223917991

Abstract: A novel machine learning model, eXtreme Gradient Boosting (XGBoost), was used for the purpose of evaluating the moment capacity of cold-formed steel (CFS) channel beams with edge-stiffened web holes subject to bending. A total of 1,620 data points were generated for training the XGBoost model, using an elasto-plastic finite element model which was validated against 12 sets of test data taken from the existing literature. The R2 score of XGBoost predictions for the moment capacity was around 99%. The performance of current design equations was evaluated through the comparison of their results against those obtained from the XGBoost model. The moment capacities obtained from the XGBoost testing dataset were also compared with that determined from the existing design equations for un-stiffened holes (USH) and edge-stiffened holes (ESH). The moment capacities determined from the current design equations for USH and ESH were found to be excessively conservative by 38.3%, and unconservative by 36.2% on average, respectively. Therefore, new design equations were proposed based on the results of parametric study using the XGBoost model. In the detailed parametric analysis, the effects of web depth, section thickness, and beam length on the moment capacity of channel beams (CFSCB) with ESH were considered. From the results of XGBoost outputs, the absolute percentage error of new design equations for that

based on the strengths of unperforated CFSCB was 8.78%, and for that based on the strengths of CFSCB with USH, the absolute percentage error was 13.7%. Additionally, a reliability analysis was performed to evaluate the accuracy of the proposed equations that were used to predict the moment capacity of CFS channel beams with ESH subject to bending. The reliability indices of all the proposed equations were greater than 2.5 which can be reliabie as per the guidelines of AISI.

Keywords: Cold-formed steel, moment capacity, edge-stiffened web holes, finite element analysis, machine learning, Proposed design equations.

1 Introduction

The use of cold-formed steel (CFS) members in structural engineering is increasing because of their high strength to weight ratio and for ease of installation [1-8]. CFS channel beams (CFSCB) have been used as major structural members in engineering applications (Fig. 1). These beams usually have holes that are perforated on the web to accommodate plumbing and heating services, and such web holes are often un-stiffened (Fig. 2(a)). The spacing and dimensions of un-stiffened holes (USH) are generally limited as they impact directly on the moment capacity of such CFSCB with USH. In recent times, a new generation of CFSCB with edge-stiffened holes (ESH) (Fig. 2(b)) designed by Howick Ltd. [9] have been widely used in New Zealand. However, current design standards such as the American Iron and Steel Institute (AISI) [10] and the Australian and New Zealand Standards (AS/NZS) [11] do not provide guidance for predicting the moment capacity of such CFSCB with ESH. Only Yu [12] proposed a design equation to calculate the moment capacity of CFSCB, but Yu's [12] equation was for CFSCB failing only in local buckling failure mode, without considering other buckling failure modes. Furthermore, no test data was used to validate Yu's equation. More importantly, the equations for lateral-torsional buckling as well as distortional buckling of CFSCB with ESH were not addressed [12].

Fig. 1 CFSCB as the primary load-carrying members in floor systems [13]

(a) CFSCB with USH

(b) CFSCB with ESH

Fig. 2 CFSCB with web holes considered in this study [13]

In this study, validated finite element (FE) models and 1,620 new FE results are presented. Meanwhile, the use of machine learning for the prediction of the moment capacity of CFSCB with ESH subject to bending is illustrated.

Limited research has been conducted with regards to CFSCB with ESH subject to various loading conditions. Concerning the studies on the bending behaviour of CFSCB with ESH, Yu [12] numerically investigated the influence of ESH on the moment capacity of CFSCB. The moment capacity was seen to improve by 14% on average in comparison with that of a channel section having a plain web. Experimental investigations were carried out on the cold-formed steel (CFS) single channel beams with ESH [13] and on CFS back-to-back channel beams with ESH [14], respectively. In terms of the compression behaviour of CFSCB with ESH, Chen et al. [15-17] and Chi et al. [18] carried out experimental and

numerical investigations on the behaviour of such CFS stiffened channels subject to axial force. It was revealed that the compression capacity of CFSCB with ESH was higher than that with a plain web. Based on the outcomes reported by Chen et al. [15-17], extensive studies were presented by Fang et al. [19] with the application of a deep belief network (DBN) trained by around 50,000 data points to obtain the compression capacity of CFS channel columns with ESH. These data points were generated from elasto-plastic FE models which incorporated residual stresses and initial geometric imperfections [19]. Regarding the web crippling behaviour, the bearing capacity of CFSCB with ESH was demonstrated to be almost as much as that of CFSCB with a plain web, both subject to One-Flange loading [20] and Two-Flange loading [21-23]. In relation to the shear behaviour, experimental research was performed by Chen et al [24] to study the shear behaviour of CFSCB with ESH. The results of CFSCB with USH obtained from the AISI [10] and AS/NZS [11] were found to be unconservative by 7% in comparison with that of CFSCB with ESH. Kanthasamy et al. [25] numerically validated the test results of Chen et al. [13], and then carried out parametric studies to investigate the shear capacity of doubly symmetric beams having circular ESH. The edge-stiffener length was recommended to be set as 15 mm and modified design equations were proposed over the existing Direct Strength Method (DSM) design rules.

Many studies on CFSCB with USH are available in the literature. Regarding the web crippling behaviour, the effects of web perforations were studied under different loading cases [26-29]. For the case of bending behaviour, Zhao et al. [30] conducted tests to study the moment capacity of CFSCB with USH and showed how the DSM in AISI [10] predicted the moment capacity of CFSCB with USH in an unconservative approach. Similarly, Moen et al. [31, 32] tested the moment capacity of CFSCB with USH, then the modified DSM equations which considered the effects of USH were proposed to obtain the moment capacity of such beams. The distortional buckling capacity of CFSCB with USH was analytically studied by

Yu et al. [33, 34]. The effects of slotted holes on the moment capacity of CFSCB were investigated by Degtyareva et al. [35, 36]. Pham [37] and Ishqy et al. [38] investigated the shear capacities of CFSCB with circular holes. In addition, Pham et al. [39-41] studied the shear capacities of CFSCB with square [39], rectangular [40] and elongated holes [41]. In terms of compression behaviour, Kulatunga et al. [42, 43] conducted an experimental study on the buckling behaviour of CFS channel columns by considering the effect of hole shapes using circular USH and elongated USH. The applicability of the DSM to obtain the compression capacity of CFS columns with USH was examined by Moen and Schafer [44, 45].

Machine learning (ML) is a useful tool for identifying useful data features [46]. There has been a recent rise in interest to apply data-driven or ML approaches to estimate the complex underlying relationships [47-50]. When an Artificial Intelligence (AI) algorithm is used to model structural members, two main issues may arise: the first is to convert the input features to the numerical data that the approach can use, which is the most critical step in arbitrary AI algorithm; and the second is to determine the most appropriate topology to evaluate the prediction problem [51, 52]. There are numerous engineering applications of ML predictions. Mangalathu et al. [53] established the seismic failure mode in reinforced concrete shear walls using eight machine learning models including Naïve Bayes, Decision Tree, Random Forest, K-Nearest Neighbors, AdaBoost, LightGBM, CatBoost, and XGBoost models. Recently, the behaviours of CFS members were investigated by Fang et al. [54, 55] using DBN.

XGBoost is an efficient machine learning method developed by Chen and Guestrin [56]. The main advantage of XGBoost in comparison with the standard machine learning algorithms is the faster computational capacity. Chen and Guestrin [56] found that the computational end-to-end costs including data loading can be ten times lesser than other

machine learning methods in general when using 1.7 billion examples. The second advantage of XGBoost compared to other machine learning methods is the higher accuracy. To investigate the accuracy of different machine learning methods, Fang et al. [19] and Degtyarev and Tsavdaridis [57] evaluated the performance perforated steel beams using various machine learning methods, comprising DBN, XGBoost, Decision Tree, Random Forest, K-Nearest Neighbors, LightGBM and CatBoost. It was proven that XGBoost provided the best prediction results for both training and testing datasets.

Previous research mainly used experimental tests, finite element analysis (FEA), and some basic machine learning algorithms to study the behaviours of perforated CFS members. Compared to FEA, machine learning method is faster and more convenient. This study aims to provide a new XGBoost framework that can predict the moment capacity of CFSCB with ESH. Additionally, the current design standards don't include any guidance for determining the moment capacity of CFSCB with ESH. As a result, new design equations were proposed. A nonlinear elasto-plastic FE model was first developed and then validated with the test data available in the literature. To train the XGBoost model, a total of 1,620 data points were acquired based on the validated FE model. The test data was divided into two parts: input data and output data. ML models comprising XGBoost and Linear Regression were then utilised to predict the results and to obtain the absolute percentage errors so that the accuracy of the various techniques could be determined. When XGBoost predictions were compared with the moment capacity of stiffened CFSCB calculated as per the AISI [10], AS/NZS [11] and Yu [12], the XGBoost model was found to perform better than the current design equations. The influences of various parameters on the moment capacity of CFSCB with ESH were also investigated. Furthermore, design equations used for the prediction of the moment capacity of CFSCB with ESH subject to bending were proposed using the data obtained from the XGBoost model. Finally, a reliability analysis was performed to evaluate the reliability of

the proposed design equations for predicting the moment capacity of cold-formed steel channel beams with edge stiffened web holes.

2 Summary of test results reported by Chen et al. [13]

Chen et al. [13] tested the behaviour of CFSCB with ESH subject to 4-point bending. Fig. 3 shows the schematic drawing of this test. The moment capacity of CFSCB with ESH was investigated with various hole sizes and hole spacings. The test specimens included both single hole channels and channels with multiple holes placed with different spacings. In total, 12 specimens were tested which included channels with both edge-stiffened and un-stiffened holes. The test results of Chen et al. [13] were utilised in this study to validate the FE models developed herein.

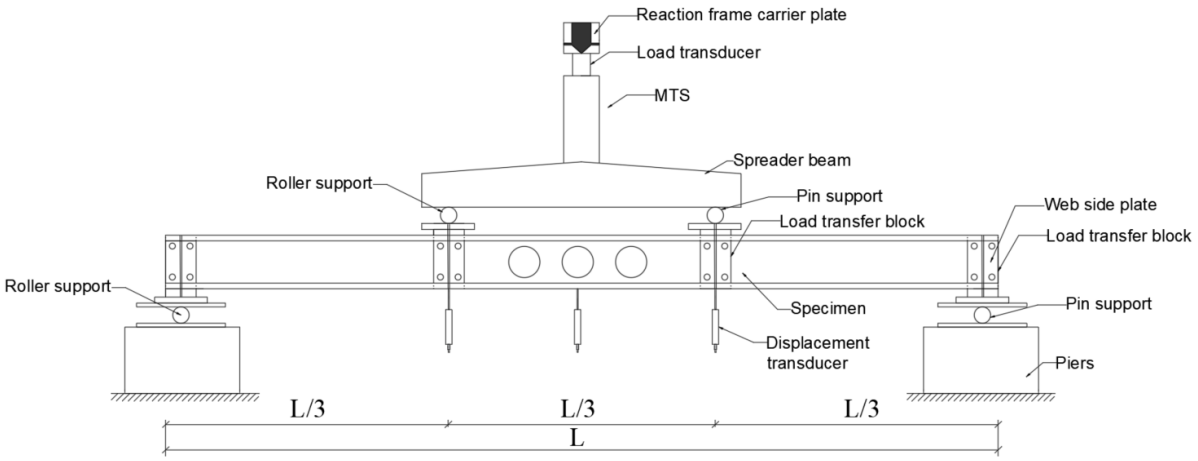

Fig. 3 Schematic drawing of 4-point bending tests conducted by Chen et al. [13]

3 Finite element analysis

3.1 Material model

ABAQUS [58] was used to develop nonlinear elasto-plastic FE models to obtain the moment capacity of CFSCB with ESH. The measured section dimensions and material parameters obtained from the tensile coupon tests [13] were used to develop FE models. The true material curve was converted from the engineering one with the help of Equations (1) and (2) [58].

$$\sigma_{true} = \sigma(1+\varepsilon) \tag{1}$$

$$\varepsilon_{true} = \ln(1+\varepsilon) - \frac{\sigma_{true}}{E} \tag{2}$$

where, E represents the Young's modulus; σ_{true} and ε_{true} represent the true stress and strain, respectively; σ and ε represent the engineering stress and strain, respectively.

Figs. 4(a) and 4(b) show the engineering curves of Section 240 and Section 290, respectively. Both flat and corner coupons were tested, and three tensile coupon tests were conducted for different types of coupons, comprising flat coupons and corner coupons of both Section 240 and Section 290.

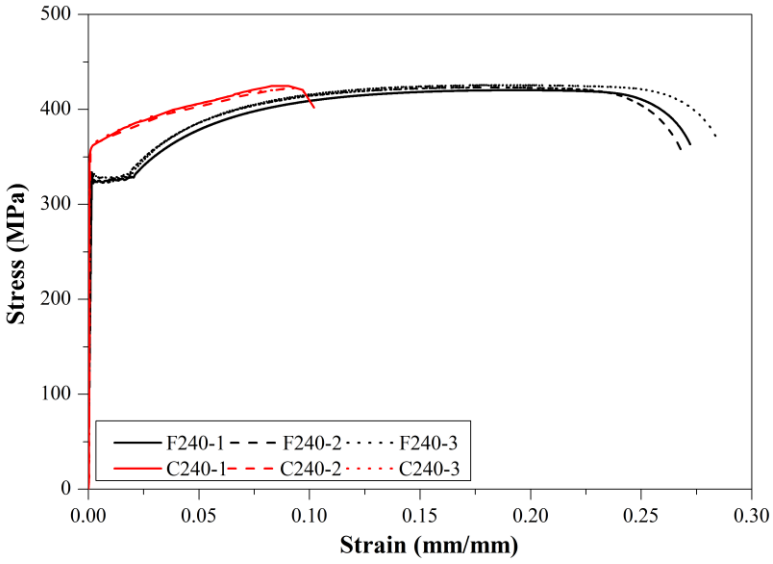

(a) Section 240

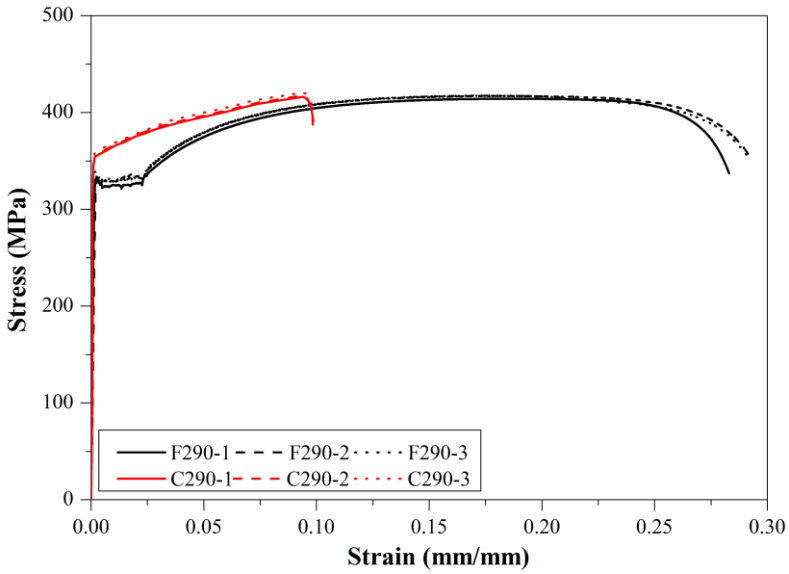

(b) Section 290

Fig. 4 Engineering stress-strain curves

The average curves of each type of Section 240 flat coupons and corner coupons were presented by Chen et al. [13]. Fig. 5 shows the engineering and true stress-strain curves of Section 240.

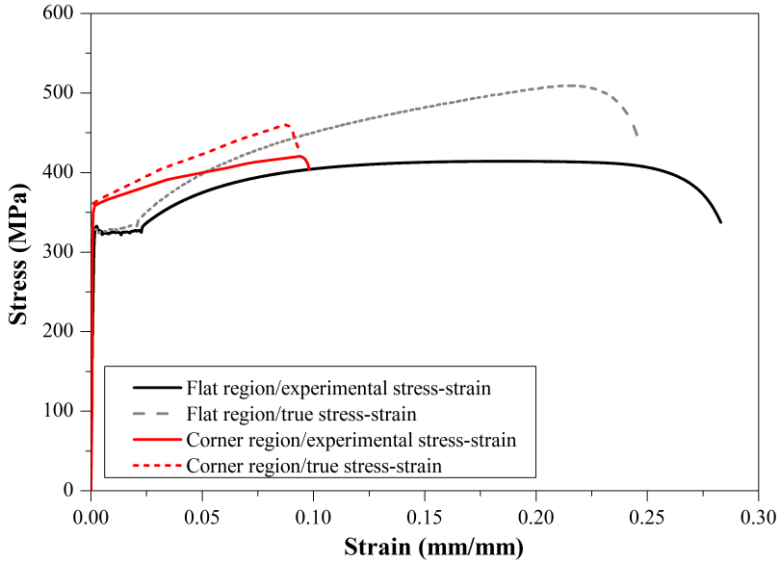

Fig. 5 Stress-strain curves of flat and corner coupons (Section 240) [13]

The material properties were reported by Chen et al. [13] as shown in Table 1. The material properties determined from testing of flat coupons and corner coupons were assigned to the FE models in the corresponding regions.

Table 1 Material properties obtained from tensile coupon tests [13]

Coupons	Coupon type	Thickness *t*/mm	Young's modulus *E* / MPa	Yield stress $\sigma_{0.2}$ / MPa	Ultimate stress σ_u / MPa
F240	Flat coupon	1.83	192057	332.8	420.5
C240	Corner coupon	1.82	210052	363.4	431.8
F290	Flat coupon	2.11	196136	330.7	415.8
C290	Corner coupon	2.13	211003	362.2	430.5

3.2 Element type and mesh size

The FE models of CFSCB were developed using S4R shell elements. The sensitivity analysis of the mesh size was performed. The FE models with four different mesh sizes were developed for W240-L4-EH3, comprising 5 mm×5 mm (width by length), 15 mm×15 mm, 30 mm×30 mm, and 50 mm×50 mm. Based on the results of the mesh sensitivity analysis (see Table 2), a 5 mm×5 mm mesh size (width by length) was chosen for CFSCB in terms of numerical accuracy.

Table 2 The moment capacity of W240-L4-EH3 using different mesh sizes

Mesh sizes (mm)	Moment capacity of FEA (kN·m)	Test strength (kN·m)
5 mm×5 mm	13.39	13.3
15 mm×15 mm	13.46	
30 mm×30 mm	13.54	
50 mm×50 mm	13.48	

As shown in Fig. 6, finer mesh sizes were assigned around the round corners to more accurately predict the moment capacity of CFSCB with ESH.

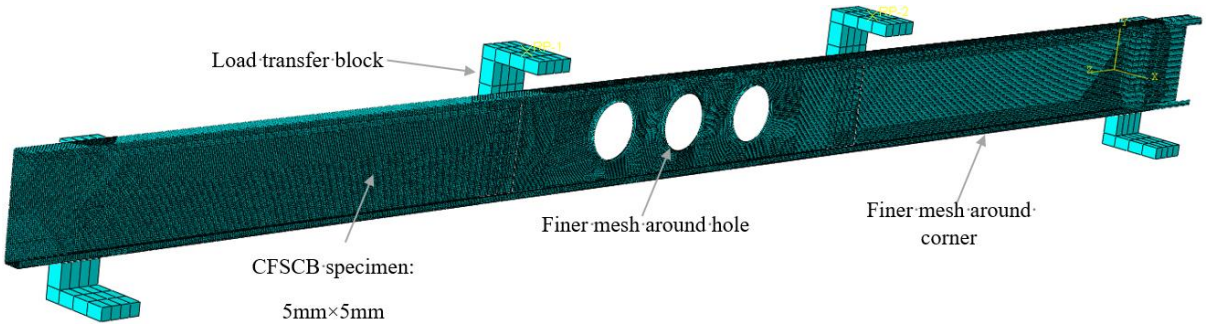

Fig. 6 Typical finite element mesh for W240-L4-EH3

3.3 Boundary conditions and loading procedure

The loads and reaction forces were transferred from the U-shaped blocks to the test specimens. As a result, in the FE models, "Surface-to-surface" interaction was applied to simulate the contacts between CFSCB webs and U-shaped blocks, and "Hard contact" in the normal direction was set to prevent any possible penetration between the two surfaces. The screws and bolts were simulated utilising multi-point constraint beam connectors instead of modelling the actual fasteners.

The boundary condition of the end roller supports was simulated through the release of in-plane rotation and displacement in the direction of the beam length. Reference nodes were assigned at the middle point of the top surface on the U-shaped block, and vertical displacements were applied on the reference nodes. The "Static General" analysis type was set for the simulation of bending tests in ABAQUS [58]. The large displacements of elements were simulated in the FE analysis by activating the "*NLGEOM" option in ABAQUS. Fig. 7 shows more details of the boundary and loading conditions used in the FE model for W240-L4-EH3. The label "W240-L4-EH3" means the web depth, length and the number of edge-stiffened holes as 240 mm, 4 m and 3, respectively. Similar FE modelling techniques for CFS beams were reported in [59-65].

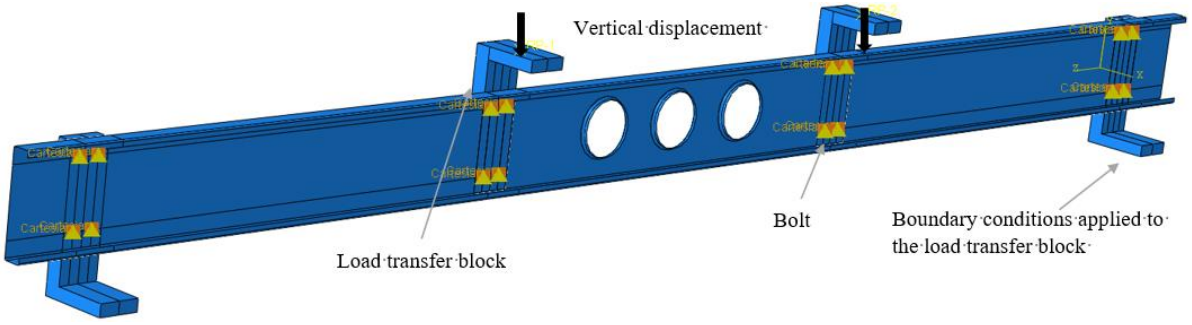

Fig. 7 Boundary condition applied to the FE model of W240-L4-EH3

3.4 Modelling of initial geometric imperfections

In the FE models, initial geometric imperfections were considered. Local and lateral-torsional geometric imperfections were taken into consideration. For each CFSCB with ESH, a buckling analysis was performed to obtain the eigenvalues and eigenmodes, and the lowest eigenmode was applied to each model. The magnitudes of local and lateral-torsional imperfections of CFSCB with ESH were scaled to the values obtained from the tests for validation purpose and then for the other FE models, the magnitudes of imperfections were taken from the recommendations of AS/NZS (2018) [11]. Similar techniques to model initial geometric imperfections were also used by Ye et al. [66] and Gatheeshgarm et al. [67]. Fig. 8 shows the initial geometric imperfection contours of local and lateral-torsional buckling modes. Additionally, the maximum amplitudes of all imperfections can be found in Chen et al. [13].

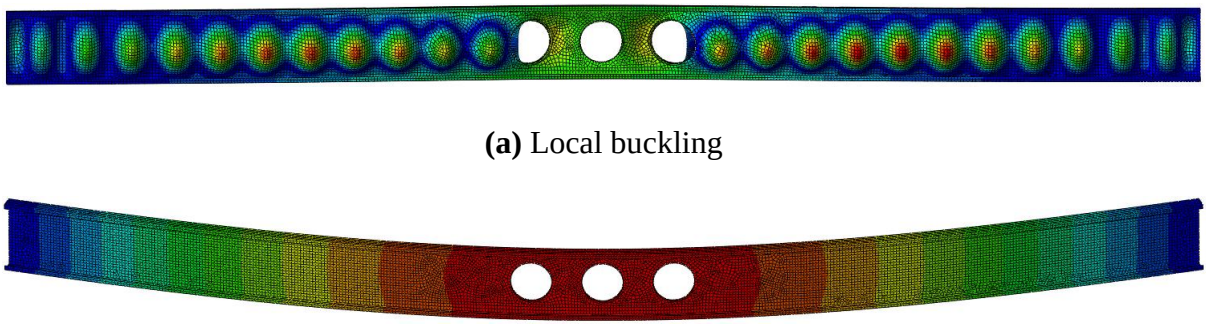

(a) Local buckling

(b) Lateral-torsional buckling

Fig. 8 Initial geometric imperfection contours for W240-L4-EH3

3.5 Validation of FE models

The moment capacities obtained from the FEA were compared with the test data reported by Chen et al. [13]. Table 3 shows the comparison results. The eigen values are presented in Table 3. In the eigenvalue analysis, a unit force (1 N·m) in the *y*-axis was applied to the top surface of load transfer blocks (Fig. 7). The value of the ratio of the test to FEA moment capacities (M_{TEST}/M_{FEA}) is 1.01 on average, and the coefficient of variation (COVs) is 0.03. It can be seen from Table 3 that the FEA results are quite close to the test

data. The deformed shapes of the sections, as obtained from the FEA, are shown in Fig. 9, and they match closely with the experimentally obtained failure modes. Fig. 10 compares the test data with FEA results which considered different factors comprising corner enhancement, residual stress, and initial geometric imperfections. Generally, the developed FE models could accurately predict the results acquired from Chen et al. [13]. It was found that the residual stresses have negligible effects on the bending capacity of CFSCB with ESH. The negligible effects of residual stresses were also reported in [68-70]. Therefore, residual stresses were not included in the FE models.

Table 3 Moment capacity of CFSCB obtained from the tests [13] and FEA

Specimen	Web depth b_w (mm)	Thickness t (mm)	Hole spacing s (mm)	Moment capacity of tests [13] M_{TEST} (kN·m)	Moment capacity of FEA M_{FEA} (kN·m)	Eigen value	M_{TEST}/M_{FEA}
CFSCB with ESH							
W240-L4-EH1	240.8	1.85	-	12.9	12.97	7326	0.99
W240-L4-EH3	240.2	1.80	100	13.3	13.39	7639	0.99
W240-L4-EH5	240.6	1.81	50	13.7	13.93	7722	0.98
W290-L4-EH1	290.8	2.13	-	19.3	18.31	8408	1.05
W290-L4-EH3	290.3	2.15	100	19.8	19.12	8655	1.04
W290-L4-EH5	291.2	2.10	50	20.5	19.98	8635	1.03
CFSCB with USH							
W240-L4-UH1	241.6	1.82	-	11.0	11.75	6643	0.94
W240-L4-UH3	239.8	1.80	100	10.6	10.85	6853	0.98
W240-L4-UH5	239.6	1.81	50	10.2	10.17	6645	1.00
W290-L4-UH1	290.9	2.16	-	16.7	16.75	7353	1.00
W290-L4-UH3	290.0	2.11	100	16.3	15.46	7470	1.05
W290-L4-UH5	290.5	2.10	50	15.7	15.19	7348	1.03
Mean							1.01
COV							0.03

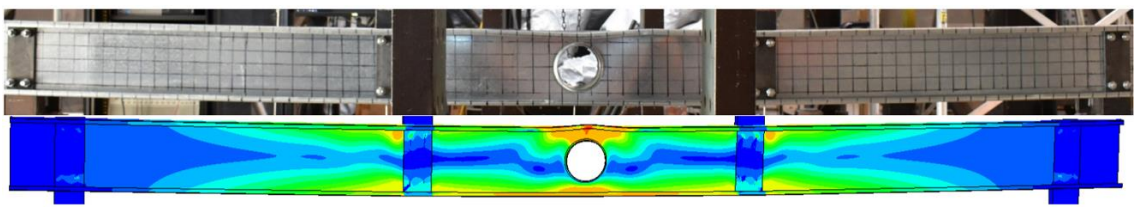

(a) W240-L4-EH1

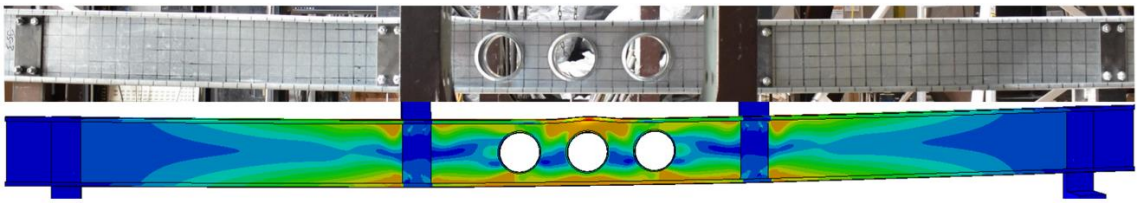

(b) W240-L4-EH3

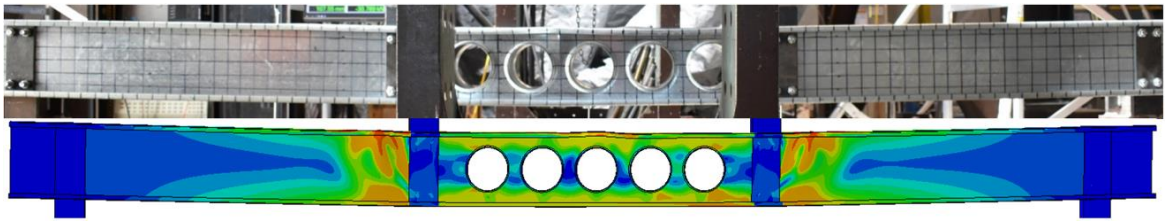

(c) W240-L4-EH5

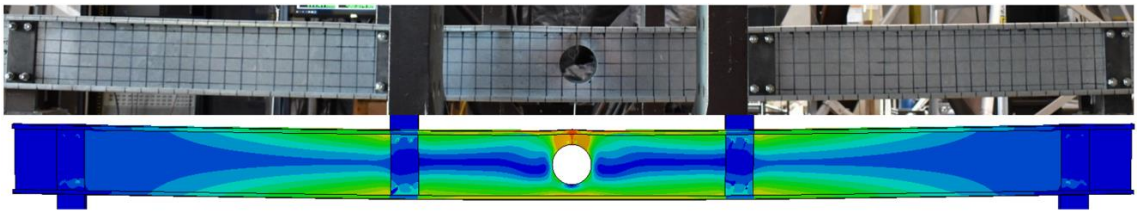

(d) W240-L4-UH1

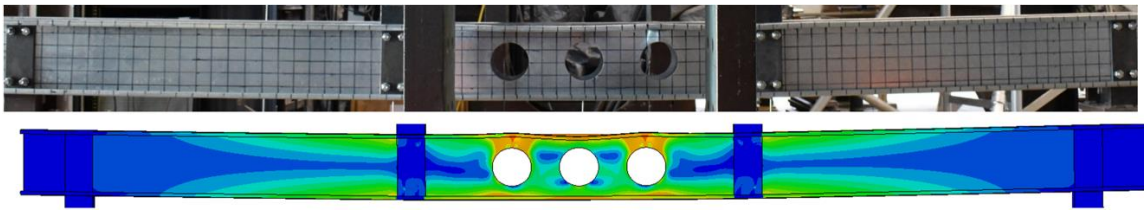

(e) W240-L4-UH3

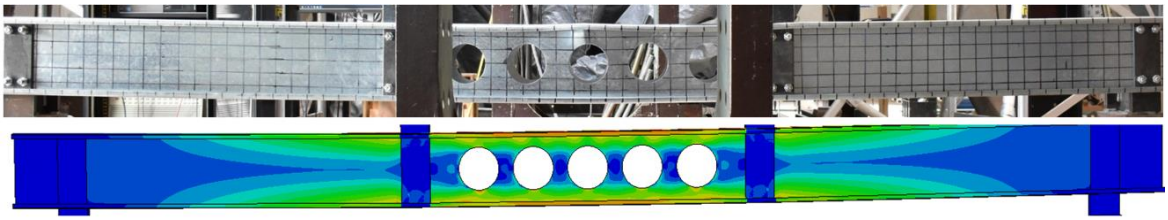

(f) W240-L4-UH5

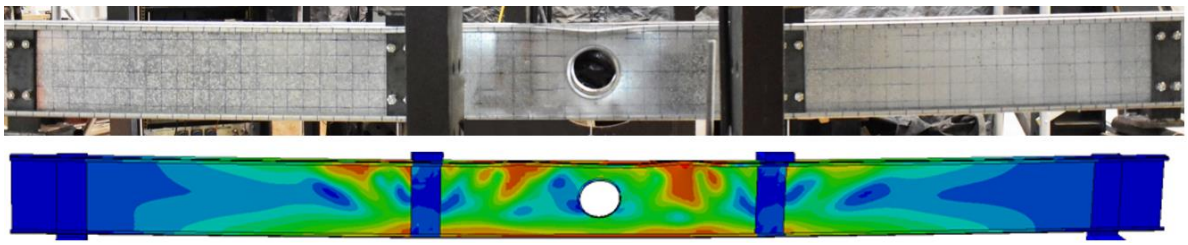

(g) W290-L4-EH1

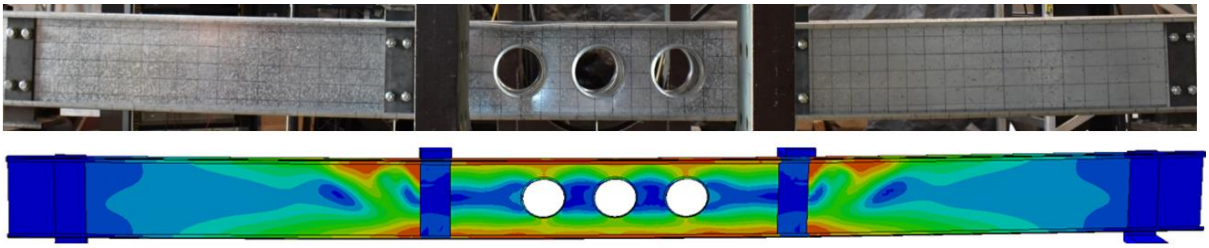

(h) W290-L4-EH3

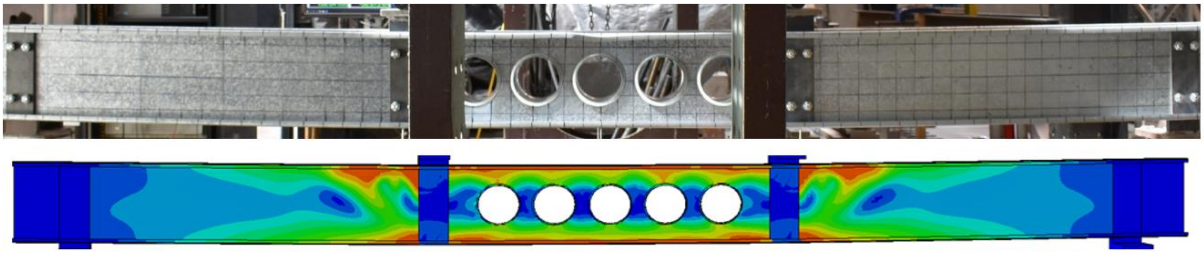

(i) W290-L4-EH5

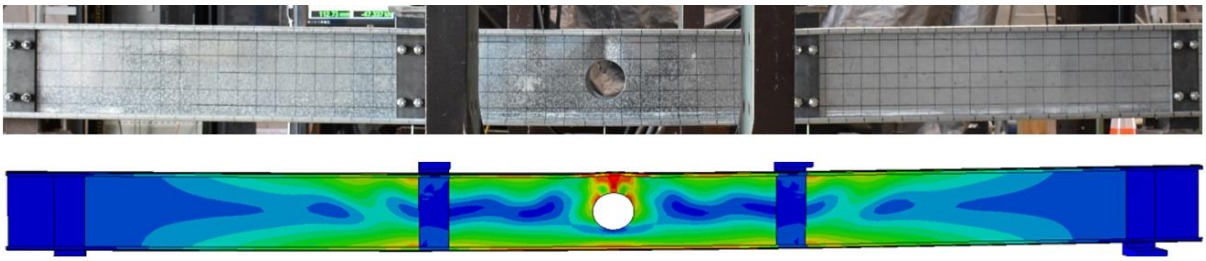

(j) W290-L4-UH1

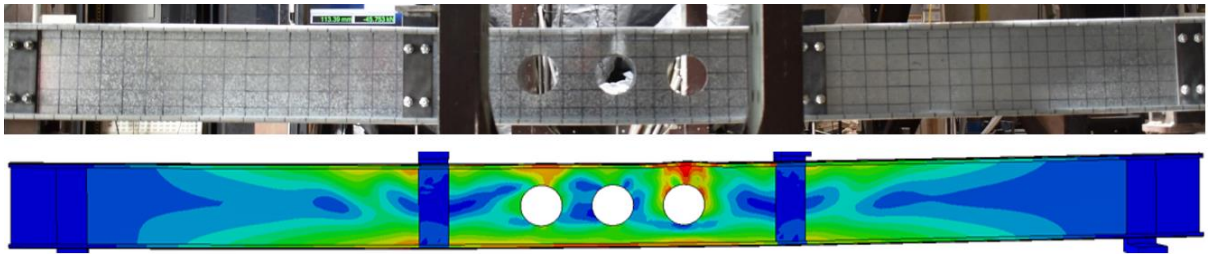

(k) W290-L4-UH3

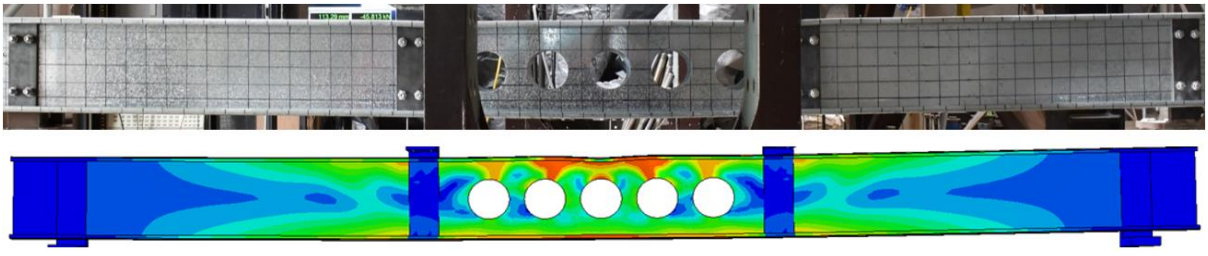

(l) W290-L4-UH5

Fig. 9 Deformed shapes at failure from experiments [13] and FEA

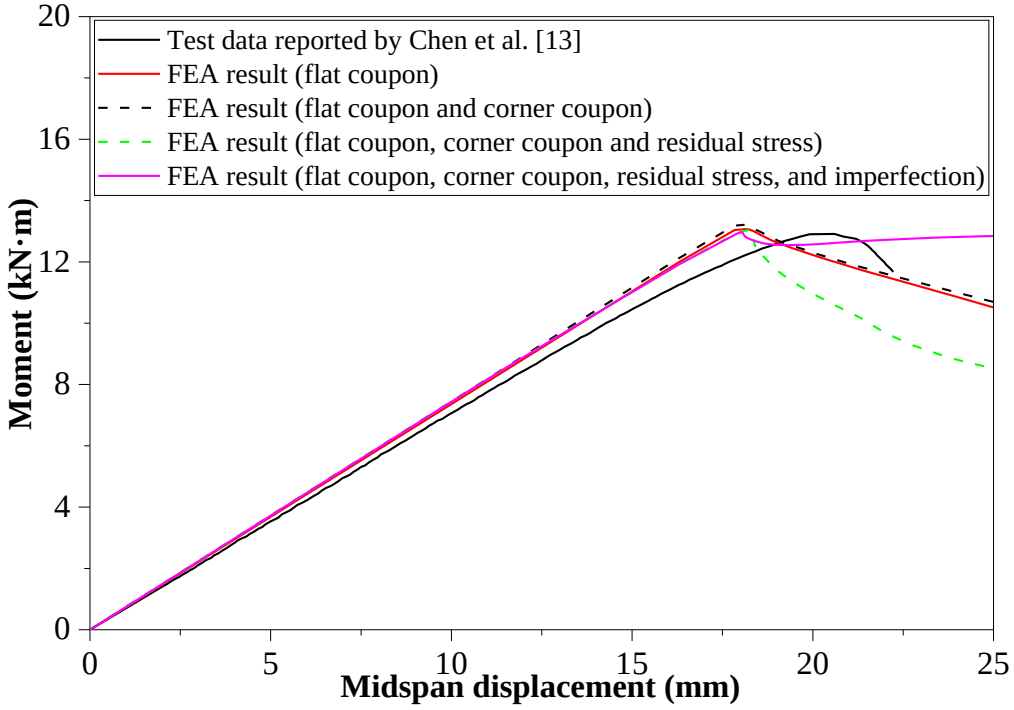

(a) W240-L4-EH1

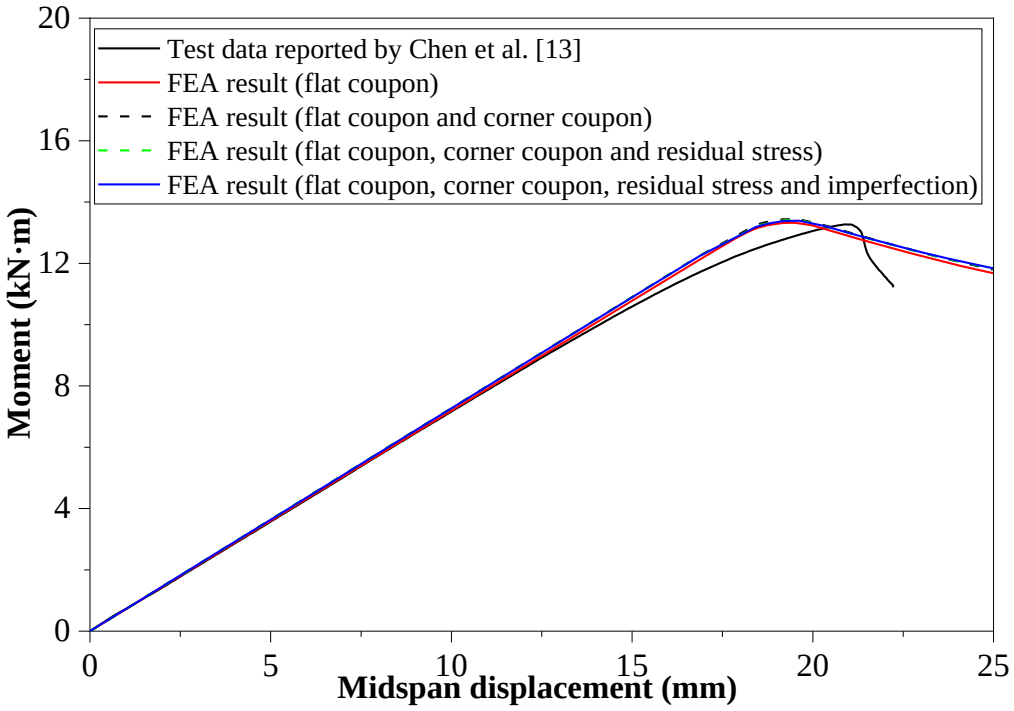

(b) W240-L4-EH3

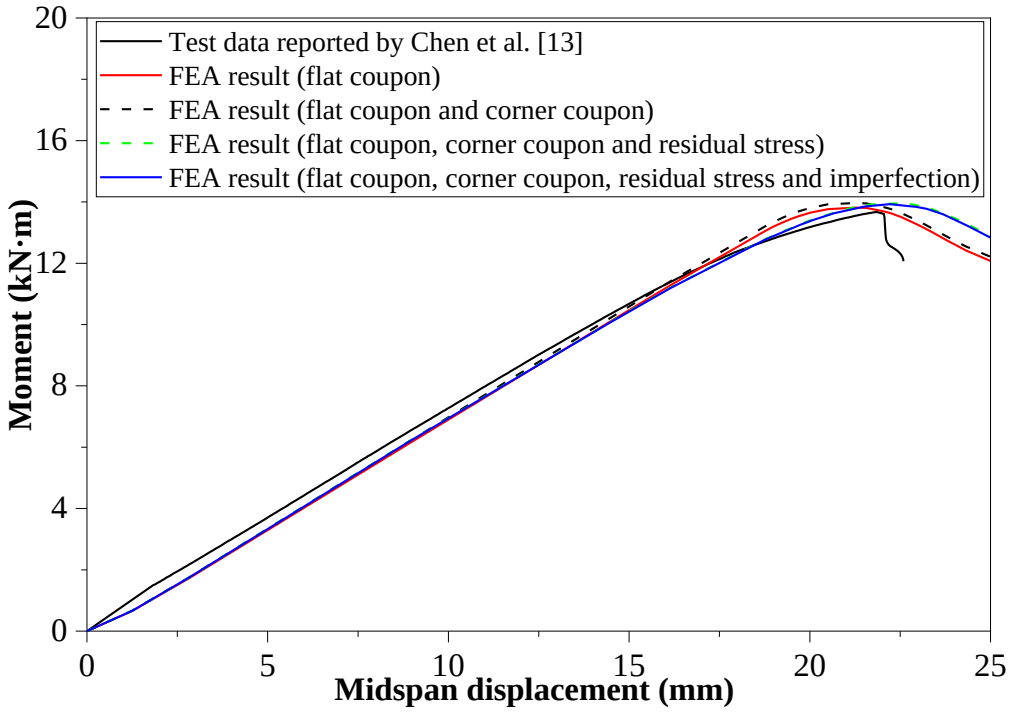

(c) W240-L4-EH5

Fig. 10 Comparison of results obtained from the tests (Chen at al.) and the FEA developed herein, in terms of moment-displacement curves

4 Current design rules

4.1 Design formulae for calculating flexural capacity of CFSCB with USH [31, 32]

4.1.1 Moment capacity for lateral-torsional buckling

The "weighted average" approach recommended by Moen and Schafer [31, 32] was used to obtain the lateral-torsional buckling strength of CFSCB with USH. The classical equation of lateral-torsional stability strength (M_{cre}) for a gross section is shown in Equation (3).

$$M_{cre} = \frac{\pi}{L}\sqrt{EI_y(GJ + EC_w\frac{\pi^2}{L^2})} \quad (3)$$

where I_y is the moment of inertial in short axis; G is the elastic shear modulus; J is the torsion constant; and C_w is the warping constant.

To calculate the lateral-torsional buckling strength of CFSCB with USH, I_y, J and C_w should be replaced by I_{yavg}, J_{avg} and C_{wavg}. C_{wavg} can be obtained by reducing the section thickness to zero within the region of the hole diameter. I_{yavg}, and J_{avg} can be obtained from the following equations.

$$I_{yavg} = \frac{I_{yg}L_g + I_{ynet}L_{net}}{L} \quad (4)$$

$$J_{avg} = \frac{J_g L_g + J_{net} L_{net}}{L} \quad (5)$$

where I_g and I_{net} are the moment of inertial of the gross section and net section, respectively; J_g and J_{net} are the torsion constant of the gross section and net section, respectively; L_g and L_{net} are the length of the CFSCB with gross section and net section, respectively; and L is the total beam length.

4.1.2 Moment capacity for distortional buckling

The DSM equations used to obtain the moment capacity of CFSCB with USH were taken from the literature [31, 32]. The nominal moment capacity for distortional buckling (M_{bd}) of CFSCB with USH was determined using Equations (6)-(12):

For $\lambda_d \le \lambda_{d1}$, $M_{bd} = M_{ynet}$ (6)

For $\lambda_{d1} < \lambda_d \le \lambda_{d2}$, $M_{bd} = M_{ynet} - (\frac{M_{ynet} - M_{d2}}{\lambda_{d2} - \lambda_{d1}})(\lambda_d - \lambda_{d1})$ (7)

For $\lambda_d > \lambda_{d2}$, $M_{bd} = [1 - 0.22(\frac{M_{crd}}{M_y})^{0.5}](\frac{M_{crd}}{M_y})^{0.5} M_y$ (8)

$$\lambda_d = \sqrt{\frac{M_y}{M_{crd}}} \quad (9)$$

$$\lambda_{d1} = 0.673(\frac{M_{ynet}}{M_y})^3 \quad (10)$$

$$\lambda_{d2} = 0.673(1.7(\frac{M_y}{M_{ynet}})^{2.7} - 0.7) \quad (11)$$

$$M_{d2} = (1 - 0.22(\frac{1}{\lambda_{d2}}))(\frac{1}{\lambda_{d2}})M_y \quad (12)$$

where M_{crd} represents the critical elastic distortional buckling moment comprising hole effects; M_y represents the member yield moment ($M_y = Z_f \times f_y$); M_{ynet} represents the member yield moment of the net section ($M_{ynet} = Z_{fnet} \times f_y$); Z_f and Z_{fnet} are the section modulus of the gross section and net section, respectively; f_y represents the CFS yield strength.

The elastic distortional buckling moment of CFSCB with USH can be obtained from the following equation.

$$M_{crd} = \min(M_{crdg}, M_{crdn}) \quad (13)$$

where, M_{crdg} is the critical elastic buckling moment for a distortional buckling half-wavelength occurring in the gross section, and M_{crdn} is the critical buckling moment for a distortional buckling half-wavelength in the net section. M_{crdn} can be obtained from the THIN-WALL-2 software which can be used to conduct finite strip analysis, where the section thickness should be replaced by reducing the web thickness from t to t_r determined by Equation (14).

$$t_r = (1 - \frac{L_h}{L_{crd}})^{1/3} t \quad (14)$$

where t is the section thickness; L_h is the overall hole length in a distortional buckling half-wavelength; L_{crd} is the distortional buckling half-wavelength of the CFSCB with gross section [31, 32].

4.1.3 Moment capacity for local buckling

The nominal moment capacity for local buckling (M_{bl}) of CFSCB with USH was determined by Equations (15) and (16) as given next.

For $\lambda_l \le 0.076$, $M_{bl} = M_{be} \le M_{ynet}$ (15)

For $\lambda_l > 0.076$, $M_{bl} = [1 - 0.15(\frac{M_{crl}}{M_{be}})^{0.4}](\frac{M_{crl}}{M_{be}})^{0.4} M_{be} \le M_{ynet}$ (16)

where, M_{bl} is the nominal moment capacity due to local buckling; M_{be} is the nominal moment capacity due to lateral-torsional buckling; M_{crl} is the critical elastic local buckling moment considering hole effects.

Moen and Schafer [31, 32] proposed a method for calculating the elastic local buckling moment (M_{crl}) that takes hole effects into account, as given in Equation (17):

$$M_{crl} = \min(M_{crlg}, M_{crlh}) \quad (17)$$

where, M_{crlg} is the critical elastic local buckling moment at the gross section, and M_{crlh} is the critical local buckling moment at the net section.

4.2 Design formulae for CFSCB with stiffened web holes [12]

Equations (18) and (19) which were used to predict the nominal local buckling strength M_{bl} of CFSCB with ESH, which were proposed by Yu [12] on the basis of finite element results.

For $\lambda_l \le 0.925$, $M_{bl} = M_y$ (18)

For $\lambda_l > 0.925$, $M_{bl} = [1 - 0.05(\frac{M_{crl}}{M_y})^{0.35}](\frac{M_{crl}}{M_y})^{0.35} M_y$ (19)

where, $\lambda_l = \sqrt{\frac{M_{bl}}{M_y}}$, M_{crl} is the elastic local buckling moment capacity without considering the effects of holes, and M_y is the yield moment capacity.

5 eXtreme Gradient Boosting (XGBoost) machine learning tool

5.1 Overview

XGBoost (eXtreme Gradient Boosting) is a collection of algorithms that is built on the Boosting framework, and is extremely powerful in terms of parallelism, missing value handling, and predictive performance analysis. XGBoost has a number of advantages

including supporting efficient parallel training, fast training speed, low memory usage, high reliability, and widespread support. Apart from supporting decision trees, it can directly select many different weak learners in the weak learner model selection of the algorithm. In addition to the inherent loss of the algorithm, the regularisation component is included in the loss function. Throughout the algorithm optimisation method, the XGBoost loss function contains a more accurate second-order Taylor expansion on the error component. Parallel selection is used to determine the appropriate subtree splitting features and eigenvalues for each weak learner, similar to the process of decision tree construction. All feature values are sorted and grouped before parallel selection to simplify the previously described parallel selection. It selects the proper group size for the grouped features and utilises the CPU cache for reading acceleration. Meanwhile, it can save each grouping to numerous hard discs to boost input/output performance. Additionally, XGBoost optimises the algorithm robustness. The treatment of missing values is determined by enumerating if each missing value is stored in the left or right subtree at the present node. The approach contains L1 and L2 regularisation terms to avoid overfitting and has a greater capacity for generalisation. L1 and L2 regularisation terms have different effects on weights; Weights are encouraged to be small by L2 regularisation (controlled by the lambda term), whereas weights are encouraged to be zero by L1 regularisation (controlled by the alpha term). This is beneficial in models such as logistic regression, which requires some feature selection.

5.2 Cross validation

During the training phase, the overfitting problem frequently occurs, which means that the training data can be well fitted. However, the results obtained from the model used to predict data beyond the training data are not reliable. It is usual practise to isolate a subset of the training data from the validation data. Cross-validation, often known as round robin validation, is a technique for evaluating the model with the validation data. The original data

are divided into K groups and a validation set is created for all subsets, while using the remainder of the K-1 subset data as the training set, in order to build the K models. The validation set is divided into K models, and the cross-validation error is calculated by summing and averaging the final mean squared error (MSE). Cross-validation makes efficient use of sparse data and ensures that the evaluation results are as near to the performance of the models on the test set as feasible.

5.3 Performance evaluation

To evaluate the performance of each prediction method, the absolute percentage error ($Err_i(\%)$), coefficient of determination (R^2), mean absolute error (MAE), and the root mean square error (RMSE) were determined. The Equations (20)-(22) were used to determine each of these parameters:

$$\mathrm{Err}_i(\%) = \frac{|y_i - t_i|}{t_i} \times 100 \tag{20}$$

$$R^2 = \frac{\sum_{i=1}^{N}(y_i - \overline{y_i})(t_i - \overline{t_i})}{\sqrt{\sum_{i=1}^{N}(y_i - \overline{y_i})^2 \sum_{i=1}^{N}(t_i - \overline{t_i})^2}} \tag{21}$$

$$\mathrm{RMSE} = \sqrt{\frac{\sum_{i=1}^{N}(t_i - y_i)^2}{N}} \tag{22}$$

$$\mathrm{MAE} = \frac{\sum_{i=1}^{N}|y_i - t_i|}{N} \tag{23}$$

where, t_i and y_i represent the real and prediction output values for the subsequent output, respectively, and $\overline{t_i}$ and $\overline{y_i}$ represent the averages of the real and predicted outputs, respectively. N represents the data series.

5.4 Data training for the moment capacity prediction

To develop prediction models for the moment capacity of CFSCB with ESH, the data obtained from validated FE models were utilised. Prior to normalisation, the XGBoost's input and output data points were formulated as Equations (24) and (25):

$$\text{Input} = \{b_w, t, a, q, s, L\} \tag{24}$$

$$\text{Output} = \{P_{\text{out}}\} \tag{25}$$

To accelerate the gradient descent for the ideal solution following normalisation and to improve the accuracy, StandardScaler was used to normalise the data. It standardized a feature by subtracting the mean and then scaling it to a unit variance. This ensured that the variance of the data was equal to one in each dimension and the mean value was equal to zero.

In some dimensions, the observed results were not dominated by excessive eigenvalues. The mean and variance of the training data were determined using the fit transform, and the training data was transformed to conform to a conventional normal distribution using the estimated mean and variance.

The data was split into two groups: training data and testing data. A total of 1620 data vectors were utilised for this investigation. The database was randomly split into the training set and testing set with the ratio of 70% and 30%, respectively.

5.5 Performance measure of the developed model

The performance of the XGBoost model was evaluated in accordance with R^2, RMSE, and MAE. The value of R^2 represents the accuracy with which the proposed formulation can anticipate the data. The RMSE is referred to as the cost function. Both RMSE and MAE were used to evaluate the accuracy and quality of fit. A good predictor model has a lower RMSE and MAE and is closer to that with an R^2 value of 1.00. The performance metrics for training

and testing sets were both determined utilising a training-testing split with a 70%-30% ratio of the entire database.

A model with a high R^2 value and a low error is deemed to have a high statistical performance. As shown in Table 4, the R^2 value determined by the training set is the highest (0.9999955), while the MAE and RMSE values are 0.0087001 and 0.0132404, respectively. In the XGBoost model, the R^2, RMSE, and MAE values for the testing set are 0.9998403, 0.0829422 and 0.0459597, respectively.

The performance of XGBoost model was also checked by comparing its results with the results obtained from the Linear Regression model. As shown in Tables 4 and 5, XGBoost outperforms the prediction of the Linear Regression model by a wide margin.

Table 4 The performance measure of XGBoost model

XGBoost Training			XGBoost Testing		
R^2	RMSE	MAE	R^2	RMSE	MAE
0.9999955	0.0132404	0.0087001	0.9998403	0.0829422	0.0459597

Table 5 The performance measure of Linear Regression model

Linear Regression Training			Linear Regression Testing		
R^2	RMSE	MAE	R^2	RMSE	MAE
0.9016	1.9904	1.5166	0.8943	4.2239	1.5967

5.6 Comparison of machine-learning testing datasets with the current design strengths

The moment capacities obtained from the XGBoost testing dataset were also compared with that determined from the existing design equations proposed by Moen and Schafer [31, 32] and Yu [12]. The moment capacities determined from the design equations for USH [31, 32] and ESH [12] were found to be excessively conservative by 38.3%, and unconservative by 36.2% on average, respectively. The ratio of hole diameter to web depth considered in the machine learning testing datasets was changed from 0.1 to 0.5. For Moen and Schafer equations (USH) [31, 32], the design strengths were conservative from 36.81% to 39.83%.

For Yu equations (ESH) [12], the design strengths were unconservative from 35.65% to 37.42%.

5.7 Comparison of machine-learning predictions with the current design strengths

As shown in Fig. 11 and Table 6, the absolute error in percentage for moment capacities of CFSCB with ESH determined by the XGBoost model, Moen and Schafer equations [31, 32] and Yu equations [12] are 6.61%, 35.26%, and 42.15%, respectively. It can be found that the moment capacities of CFSCB with ESH determined by the equations proposed by Moen and Schafer [31, 32] and Yu [12] are much lower than the XGBoost predictions. Compared with the design strengths mentioned above, the XGBoost results have the best performance in predicting the moment capacity of CFSCB with ESH.

Table 6 Absolute percentage errors for the prediction of moment capacities for CFSCB with ESH

Specimen ID	Moment capacity (kN·m)	Err% (Moen and Schafer [31, 32])	Err% (Yu [12])	Err% (Proposed equations based on CFSCB)	Err% (Proposed equations based on CFSCB with USH)	Err% (XGBoost)
1 W290-L4-EH1	19.30	22.80	3.08	3.06	7.46	10.26
2 W290-L4-EH3	19.80	25.76	0.47	0.45	15.51	9.29
3 W290-L4-EH5	20.50	29.27	2.96	2.97	26.82	10.93
4 W240-L5-EH4	12.39	17.28	7.12	7.26	0.97	6.97
5 W290-L6-EH2	15.82	26.67	25.77	25.68	10.00	4.50
6 W240-L7-EH1	10.04	37.93	32.24	7.59	17.11	0.84
7 W290-L8-EH5	12.43	42.54	60.10	1.01	15.49	5.24
8 W240-L9-EH2	7.60	49.09	74.61	11.46	9.75	3.30
9 W240-L10-EH4	6.59	51.76	101.34	15.96	17.78	10.76
10 W290-L10-EH5	9.30	49.49	113.80	12.29	16.17	4.01
Mean		35.26	42.15	8.78	13.7	6.61
COV		0.35	1.01	0.89	0.51	0.53

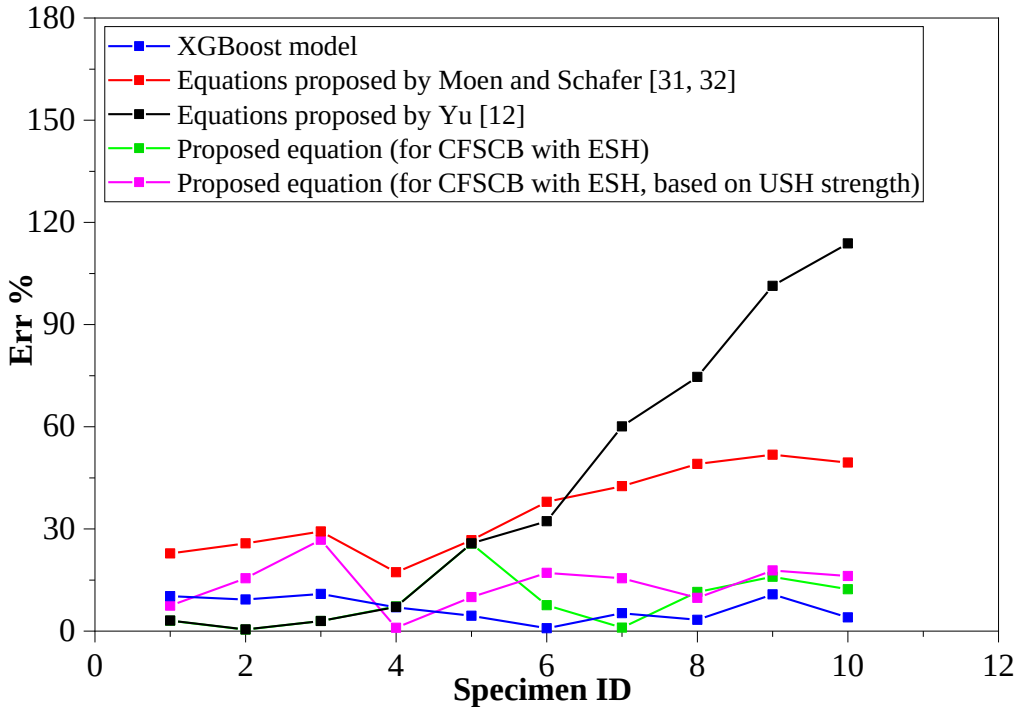

Fig. 11 Absolute percentage error for the prediction of moment capacities for CFSCB with ESH

6 Parametric study

6.1 General

The validated XGBoost model was utilised to perform a comprehensive parametric study to determine the effect of section web depth, section thickness, and beam length on the moment capacity of CFSCB with ESH subject to bending. The web depth of the section (b_w) was adjusted between 150 mm and 300 mm. The section thickness (t) was changed from 1.5 mm to 3.0 mm. The beam length (L) was varied between 4 m and 12 m. Different numbers of ESH were considered, with an equidistant hole spacing along the pure bending length of the beam.

The other parameters were kept constant in the parametric study, including flange width (45 mm), lip depth (15 mm), the ratio of hole diameter to web depth (0.1), and the ratio of stiffener length to web depth (0.04). Table 7 shows all related parameters considered in the parametric study.

Table 7 Parameters considered in the parametric study

Web depth	Flange width	Lip width	Thickness	Ratio of hole diameter to web depth	Ratio of stiffener length to web depth	Length	Stiffened hole numbers
W/mm	b_f/mm	b_l/mm	t/mm	A	Q	L/m	n
150	45	15	1.5	0.1	0.04	4	1
to			to			to	to
300			3			12	5

411 *6.2 Specimens labelling*

412 The labels of CFSCB with ESH are shown in Fig. 12. The nominal web depth, nominal
413 section thickness, the ratio of hole diameter to web depth, the ratio of stiffener length to web
414 depth, nominal beam length and the number of holes were defined in the label.

415 For instance, the label "W240-t1.5-A0.1-Q0.04-L4-EH1" can be described as below:

416 • "W240" represents the web depth in millimetres, i.e., 240 mm.

417 • "t1.5" represents to the section thickness in millimetres, i.e., 1.5 mm.

418 • "A0.1" represents to the ratio of hole diameter to web depth.

419 • "Q0.04" represents to the ratio of stiffener length to web depth.

420 • "L4" represents the nominal length of the specimen in metres, i.e., 4 m.

421 • "EH1' represents specimens with one edge stiffened hole.

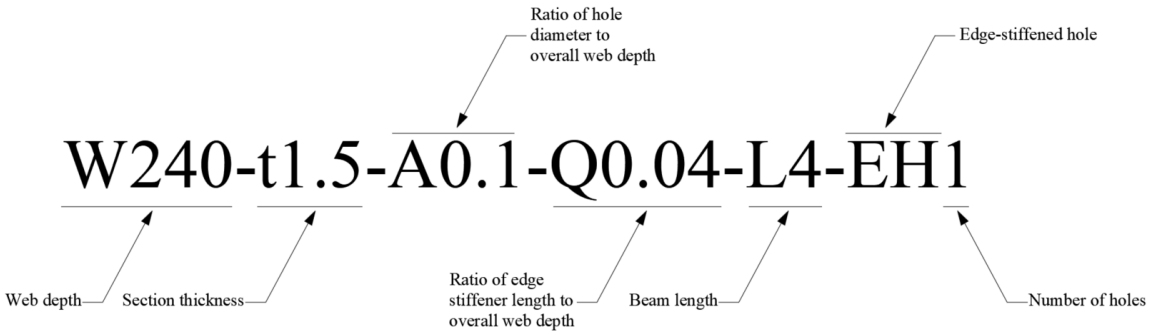

Fig. 12 Specimen labelling

422 *6.3 Results and discussion*

The influence of the web depth on the moment capacity of CFSCB with ESH is shown in Fig. 13. The mean values of the moment capacity of CFSCB with a web depth of 150 mm, 225 mm and 300 mm are 8.73 kN·m, 11.99 kN·m, and 14.43 kN·m, respectively. It can be found that an increase of 65.3% in moment capacity occurs when the web depth increases from 150 mm to 300 mm.

Fig. 14 shows the effect of section thickness on the moment capacity of CFSCB with ESH. The mean values of the moment capacity of CFSCB having the section thickness of 1.5 mm, 2 mm, 2.5 mm, and 3 mm are 6.64 kN·m, 10.01 kN·m, 13.44 kN·m, and 16.78 kN·m, respectively. It is indicated that the moment capacity has a 152% increase when the thickness of the channels changed from 1.5 mm to 3 mm. Hence, section thickness significantly affects the moment capacity of CFSCB with ESH.

The effect of beam length on the moment capacity of CFSCB with ESH was studied as well. The mean values of the moment capacity of CFSCB with a beam length of 4 m, 6 m, 8 m, 10 m, and 12 m are 17.53 kN·m, 14.81 kN·m, 11.43 kN·m, 8.44 kN·m, and 6.38 kN·m, respectively. A decrease in the moment capacity by 63.6% can be observed when the beam length is changed from 4 m to 12 m. It is indicated that the influence of beam length should be taken into consideration when calculating the moment capacity of CFSCB with ESH (Fig. 15). Lateral restraints along the beam length are recommended to be set to increase the moment capacity of slender CFSCB.

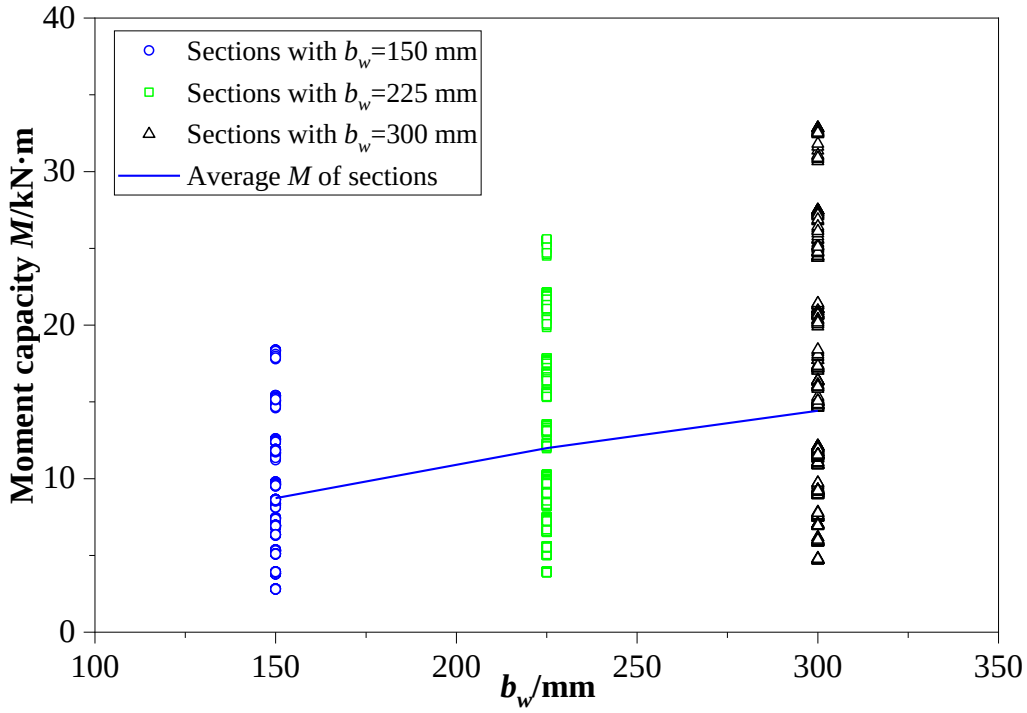

Fig. 13 Effect of web depth b_w on moment capacity

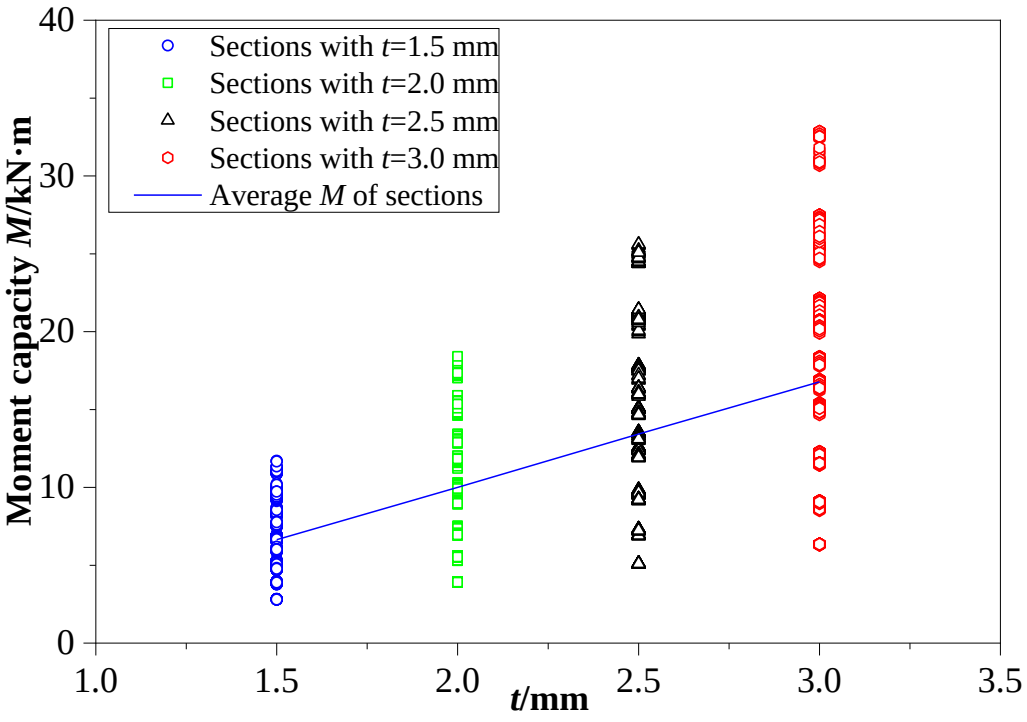

Fig. 14 Effect of section thickness t on moment capacity

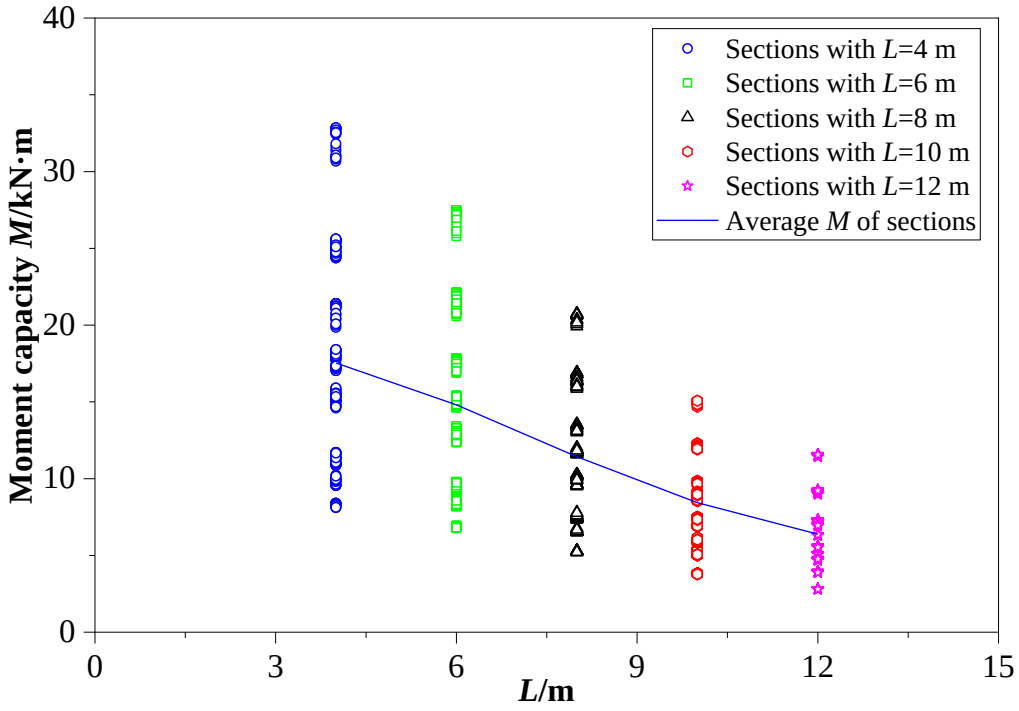

Fig. 15 Effect of beam length *L* on moment capacity

7 Proposed design equations

As mentioned before, only Yu [12] proposed design equations for the prediction of moment capacity of CFSCB with ESH. Nevertheless, no test data was used for the validation of Yu's equation and more importantly his equation was only for columns failing in local buckling and did not include other failure modes such as distortional buckling and lateral-torsional buckling. In addition, the validated XGBoost model predicted the moment capacity of CFSCB with ESH with a higher degree of precision as compared to the existing design equations. Therefore, the results derived from the XGBoost model were used to propose new design equations for predicting the moment capacity of CFSCB with ESH.

The proposed equations can only be used for channel beams with lipped flanges, as the lipped channel sections were included in the machine learning database. It should be noted that the channels with folded flanges [71-73] are not covered in this study.

7.1 Proposed equations for CFSCB with ESH

For lateral-torsional buckling failure, the moment capacity of CFSCB with ESH can be calculated using Equations (26)-(28).

When $M_{op} < 0.573M_y$, $M_{bep} = 1.7M_{op}$ (26)

When $0.573M_y \le M_{op} \le 1.25M_y$, $M_{bep} = 2M_{op} - 0.5M_y$ (27)

For $1.25M_y < M_{op}$, $M_{bep} = 1.9M_{op} - 1.44M_y$ (28)

where, M_{op} is the critical elastic lateral-torsional buckling moment of CFSCB; M_y is the member yield moment of the gross section ($M_y = Z_f \times f_y$); and M_{bep} is the proposed nominal member moment capacity for lateral-torsional buckling of CFSCB with ESH.

For local buckling failure, the moment capacity of CFSCB with ESH can be calculated using the following Equations (29)-(30).

For $\lambda_l \le 0.439$, $M_{blp} = 1.7M_{op}$ (29)

For $\lambda_l > 0.439$, $M_{blp} = [1 - 0.15(\frac{M_{olp}}{M_{op}})^{0.75}](\frac{M_{olp}}{M_{op}})^{0.75} M_y$ (30)

where, M_{blp} is the proposed nominal member moment capacity for local buckling, and M_{olp} is the elastic local buckling moment capacity of CFSCB.

For distortional buckling failure, the moment capacity of CFSCB with ESH can be calculated using Equations (31)-(32).

For $\lambda_d \le 0.873$, $M_{bdp} = M_y$ (31)

For $\lambda_d > 0.873$, $M_{bdp} = [1.25 - 0.33(\frac{M_y}{M_{odp}})^{0.5}]M_y$ (32)

where, M_{bdp} is the proposed nominal member moment capacity for local buckling failure of CFSCB with ESH, and M_{odp} is the elastic local buckling moment capacity of CFSCB.

7.2 Proposed equations for CFSCB with ESH (based on strength of CFSCB with USH)

For lateral-torsional buckling failure, the moment capacity of CFSCB with ESH can be calculated using Equations (33)-(35).

For $M_{oh} < 0.2M_{ynet}$, $M_{bep} = 3.8M_{oh} + 0.02M_{ynet}$ (33)

For $0.2M_{ynet} \le M_{oh} \le 0.4M_{ynet}$, $M_{bep} = 1.74M_{oh} + 0.45M_{ynet}$ (34)

For $0.4M_{ynet} < M_{oh}$, $M_{bep} = 1.3M_{oh} + 0.1M_{ynet}$ (35)

where, M_{oh} is the critical elastic lateral-torsional buckling moment of CFSCB with USH; M_{ynet} is the member yield moment of the net section ($M_y = Z_f \times f_y$).

For local buckling failure, the moment capacity of CFSCB with ESH can be calculated using Equations (36)-(37).

For $\lambda_l \le 0.58$, $M_{blp} = 4.2M_{oh}$ (36)

For $\lambda_l > 0.58$, $M_{blp} = [3.2 - 0.4(\frac{M_{olh}}{M_{oh}})^{0.5}](\frac{M_{olh}}{M_{oh}})^{0.5} M_{ynet}$ (37)

where, M_{blp} is the proposed nominal member moment capacity for local buckling failure of CFSCB with USH, and M_{olh} is the elastic local buckling moment capacity of CFSCB with USH.

For distortional buckling failure, the moment capacity of CFSCB with ESH can be calculated using Equations (38)-(39).

For $\lambda_d \le 0.72$, $M_{bdp} = 1.2M_{ynet}$ (38)

For $\lambda_d > 0.72$, $M_{bdp} = (1.46 - 0.5\frac{M_{ynet}}{M_{odn}})M_{ynet}$ (39)

where, M_{bdp} is the proposed nominal member moment capacity for local buckling failure of CFSCB with ESH, and M_{odn} is the elastic local buckling moment of CFSCB with USH.

The MAE values of the proposed equations are presented in Fig. 11 and listed in Table 6. It can be found that the proposed equations perform better than those proposed by Moen and Schafer [31, 32] and Yu [12]. The mean values of the absolute error in percentage for the proposed design equations of CFSCB with ESH proposed in Sections 7.1 and 7.2 are 8.78% and 13.7%, respectively.

7.3 Reliability analysis

A reliability analysis was undertaken to evaluate the performance of proposed design equations for calculating the moment capacity of CFSCB with ESH. Any proposed design equation is accounted as reliable if its reliability index (β') is not less than 2.50, as per the guidelines of AISI [10]. Equation 40 (as given below) [10] was used to calculate the reliability indices of the proposed design equations. In Equation 40, the values of M_m and V_m were taken as 1.1 and 0.1, respectively, which were determined by the mean and COV values of the material factor. The values of F_m and V_f were 1.0 and 0.05, respectively, which were determined from the mean and COV values of the fabrication factor. The value of V_q was set 0.21 which again was determined by the COV value of the load factor. C_p represents the correction factor. As shown in Tables 8 and 9, the reliability indices of all the proposed equations are greater than 2.5, which confirms that the proposed design equations can accurately predict the moment capacity of CFSCB with ESH and USH subject to bending.

$$\varphi = CM_m F_m P_m \exp(-\beta' \sqrt{V_m^2 + V_f^2 + C_p V_p^2 + V_q^2}) \quad (40)$$

Table 8 Comparison of FEA strengths and proposed design strengths for CFSCB with ESH

(a) For lateral-tortional buckling

Non-dimensional slenderness	$M_o < 0.573M_y$	$0.573M_y \le M_o \le 1.25M_y$	$1.25M_y < M_o$
Ratio of equations	M_{FEA} / M_{prop}	M_{FEA} / M_{prop}	M_{FEA} / M_{prop}
Data number	972	297	216
Mean, P_m	1.203	1.218	0.998
COV	0.104	0.075	0.029
β' [10]	3.3	3.5	2.81
φ [10]	0.85	0.85	0.85

(b) For local buckling

Non-dimensional slenderness	$\lambda_l \le 0.439$	$\lambda_l > 0.439$
Ratio of equations	M_{FEA} / M_{prop}	M_{FEA} / M_{prop}
Data number	972	513
Mean, P_m	1.198	1.007
COV	0.105	0.129

β' [10]	3.29	2.53
φ [10]	0.85	0.85

(c) For distortional buckling

Non-dimensional slenderness	$\lambda_d \le 0.873$	$\lambda_d > 0.873$
Ratio of equations	M_{FEA} / M_{prop}	M_{FEA} / M_{prop}
Data number	27	54
Mean, P_m	0.957	1.007
COV	0.008	0.027
β' [10]	2.66	2.85
φ [10]	0.85	0.85

Table 9 Comparison of FEA strengths and proposed design strengths for CFSCB with ESH

(a) For lateral-tortional buckling

	$M_o < 0.2M_y$	$0.2M_y \le M_o \le 0.4M_y$	$0.4M_y < M_o$
Ratio of equations	M_{FEA} / M_{prop}	M_{FEA} / M_{prop}	M_{FEA} / M_{prop}
Data number	756	351	109
Mean, P_m	0.984	1.056	1.918
COV	0.075	0.169	0.102
β' [10]	2.65	2.51	5.12
φ [10]	0.85	0.85	0.85

(b) For local buckling

Non-dimensional slenderness	$\lambda_l \le 0.58$	$\lambda_l > 0.58$
Ratio of equations	M_{FEA} / M_{prop}	M_{FEA} / M_{prop}
Data number	81	81
Mean, P_m	1.031	1.152
COV	0.132	0.159
β' [10]	2.59	2.84
φ [10]	0.85	0.85

(c) For distortional buckling

Non-dimensional slenderness	$\lambda_d \le 0.72$	$\lambda_d > 0.72$
Ratio of equations	M_{FEA} / M_{prop}	M_{FEA} / M_{prop}
Data number	63	180
Mean, P_m	0.959	0.96
COV	0.056	0.036
β' [10]	2.59	2.67
φ [10]	0.85	0.85

8 Conclusions

The moment capacity of CFSCB with ESH subject to bending was predicted using a novel machine learning model which was developed using the XGBoost tool. Prior to the development of the machine learning model, nonlinear elasto-plastic FE models were developed and validated against the test results available in the literature. To train the XGBoost model, a total of 1,620 data points were generated from the validated FE models. The R^2 score of XGBoost predictions for the moment capacity of CFSCB with ESH was found to be around 99%.

The moment capacities obtained from the XGBoost testing dataset were also compared with that determined from the existing design equations proposed by Moen and Schafer for USH, and Yu for ESH. These equations were used to calculate the strengths of CFSCB with USH and ESH, respectively. The moment capacities determined from the design equations for USH and ESH were found to be excessively conservative by 38.3% on average, and unconservative by 36.2% on average, respectively. The ratio of hole diameter to web depth included in the machine learning testing datasets was varied from 0.1 to 0.5. For Moen and Schafer equations (USH), the design strengths were conservative from 36.81% to 39.83%. For Yu equations (ESH), the design strengths were unconservative from 35.65% to 37.42%. Then a total of ten specimens were randomly selected for the moment capacity comparison using XGBoost, Moen and Schafer equations, and Yu equations. The absolute errors in percentage for moment capacities of CFSCB with ESH determined by the XGBoost model, Moen and Schafer equations and Yu equations were 6.61%, 35.26%, and 42.15%, respectively.

Finally, the results of XGBoost model were used to undertake a comprehensive parametric study to investigate the influence of a range of parameters comprising section web depth, section thickness, and beam length on the moment capacity of CFSCB with ESH and

USH subject to bending. As the existing design rules were not capable of accurately predicting the moment capacity of CFSCB with ESH, the results of parametric analysis were utilised to propose new design equations for predicting the moment capacity of such beams. The mean value of the absolute error in percentage for the proposed design equations of CFSCB with ESH based on the strengths of unperforated CFSCB is 8.78%, and for that based on the strengths of CFSCB with USH, the the absolute error in percentage is 13.7%. Additionally, a reliability analysis was conducted to demonstrate that the proposed design equations are reliable and can accurately predict the moment capacity of cold-formed steel channel beams with edge-stiffened and un-stiffened web holes.

Acknowledgement

The authors wish to acknowledge eResearch at the University of Auckland (particularly for the help of Mike Laverick) in facilitating this research (http://www.eresearch.auckland.ac.nz). The use of high-performance computing machines of New Zealand eScience Infrastructure (NeSI, https://www.nesi.org.nz) and the help of Callum Walley are greatly acknowledged. The contribution of Dinesh Lakshmanan Chandramohan for helping to analyse the results, and the discussion with Changheng Lu and Parsa Yazdi on the programming and machine learning are also greatly acknowledged.

References

[1] J. Ye, G. Quan, P. Kyvelou, L. Teh, L. Gardner. A practical numerical model for thin-walled steel connections and built-up members, Struct. 38 (2022) 753-764. https://doi.org/10.1016/j.istruc.2022.02.028.

[2] J. Ye, G. Quan, X. Yun, X. Guo, J. Chen. An improved and robust finite element model for simulation of thin-walled steel bolted connections, Eng. Struct. 250 (2022) 113368. https://doi.org/10.1016/j.engstruct.2021.113368.

[3] S.M. Mojtabaei, I. Hajirasouliha, J. Ye, Optimisation of cold-formed steel beams for best seismic performance in bolted moment connections, J. Constr. Steel Res. 181 (2021) 106621. https://doi.org/10.1016/j.jcsr.2021.106621.

[4] S.M. Mojtabaei, J. Becque, I. Hajirasouliha. Local buckling in cold-formed steel moment resisting bolted connections: behaviour, capacity and design, J. Struct. Eng. (ASCE), 146 (2020) 04020167. https://doi.org/10.1061/(ASCE)ST.1943-541X.0002730.

[5] H.T. Li, B. Young, Design of cold-formed high strength steel tubular sections undergoing web crippling, Thin-Walled Struct. 133 (2018) 192-205. https://doi.org/10.1016/j.tws.2018.09.005.

[6] B.W. Schafer, T. Pekoz, Computational modelling of cold-formed steel: characterizing geometric imperfections and residual stresses, J. Constr. Steel Res. 47(3) (1998) 193-210. https://doi.org/10.1016/S0143-974X(98)00007-8.

[7] H. Liang, K. Roy, Z. Fang, J.B.P. Lim, A critical review on optimization of cold-formed steel members for better structural and thermal performances. Buildings. 12 (2022) 34. https://doi.org/10.3390/buildings12010034.

[8] B. Janarthanan, S. Gunalan, M. Mahendran, Numerical modelling of web crippling failures in cold-formed steel unlipped channel sections, J. Constr. Steel Res. 158 (2019) 486-501. https://doi.org/10.1016/j.jcsr.2019.04.007.

[9] Howick Floor, Joist System. (2013) Auckland, New Zealand.

[10] American Iron and Steel Institute (AISI), North American Specification for the Design of Cold-formed Steel Structural Members AISI S100-16, 2016.

[11] Australia/New Zealand Standard (AS/NZS), Cold-Formed Steel Structures, AS/NZS 4600:2018. Standards Australia/ Standards New Zealand, 2018.

[12] C. Yu, Cold-formed steel flexural member with edge stiffened holes: Behavior, optimization, and design, J. Constr. Steel Res. 71 (2012) 210-218. https://doi.org/10.1016/j.jcsr.2011.09.008.

[13] B. Chen, K. Roy, A. Uzzaman, J.B.P. Lim, Moment capacity of cold-formed channel beams with edge-stiffened web holes, un-stiffened web holes and plain webs, Thin-Walled Struct. 2020. 157 (2020) 107070. https://doi.org/10.1016/j.tws.2020.107070.

[14] B. Chen, K. Roy, Z. Fang, A. Uzzaman, G.M. Raftery, J.B.P. Lim, Moment capacity of back-to-back cold-formed steel channels with edge-stiffened holes, un-stiffened holes, and plain webs, Eng. Struct. 235 (2021) 112042. https://doi.org/10.1016/j.engstruct.2021.112042.

[15] B. Chen, K. Roy, A. Uzzaman, G.M. Raftery, D. Nash, G.C. Clifton, P. Pouladi, J.B.P. Lim, Effects of edge-stiffened web openings on the behaviour of cold-formed steel channel sections under compression, Thin-Walled Struct. 144 (2019) 106307. https://doi.org/10.1016/j.tws.2019.106307.

[16] B. Chen, K. Roy, A. Uzzaman, G.M. Raftery, J.B.P. Lim, Parametric study and simplified design equations for cold-formed steel channels with edge-stiffened holes under axial compression, J. Constr. Steel Res. 172 (2020) 106161. https://doi.org/10.1016/j.jcsr.2020.106161.

[17] B. Chen, K. Roy, A. Uzzaman, G.M. Raftery, J.B.P. Lim, Axial strength of back-to-back cold-formed steel channels with edge-stiffened holes, un-stiffened holes and plain webs, J. Constr. Steel Res. 174 (2020) 106313. https://doi.org/10.1016/j.jcsr.2020.106313.

[18] Y. Chi, K. Roy, B. Chen, Z. Fang, A. Uzzaman, G.B.G. Ananthi, J.B.P. Lim, Effect of web hole spacing on axial capacity of back-to-back cold-formed steel channels with edge-stiffened holes, Steel Compos. Struct. 40 (2021) 287-305. https://doi.org/10.12989/scs.2021.40.2.287.

[19] Z. Fang, K. Roy, B. Chen, C.W. Sham, I. Hajirasouliha, J.B.P. Lim, Deep learning-based procedure for structural design of cold-formed steel channel sections with edge-stiffened and un-stiffened holes under axial compression, Thin-Walled Struct. 166 (2021) 108076. https://doi.org/10.1016/j.tws.2021.108076.

[20] A. Uzzaman, J.B.P. Lim, D. Nash, B. Young, Effects of edge-stiffened circular holes on the web crippling strength of cold-formed steel channel sections under one-flange loading conditions, Eng. Struct. 139 (2017) 96-107. http://dx.doi.org/10.1016/j.engstruct.2017.02.042.

[21] A. Uzzaman, J.B.P. Lim, D. Nash, K. Roy, Cold-formed steel channel sections under end-two-flange loading condition: Design for edge-stiffened holes, unstiffened holes and

plain webs, Thin-Walled Struct. 147 (2020) 106532. https://doi.org/10.1016/j.tws.2019.106532.

[22] A. Uzzaman, J.B.P. Lim, D. Nash, K. Roy, Web crippling behaviour of cold-formed steel channel sections with edge-stiffened and unstiffened circular holes under interior-two-flange loading condition, Thin-Walled Struct. 154 (2020) 106813. https://doi.org/10.1016/j.tws.2020.106813.

[23] B. Chen, K. Roy, Z. Fang, A. Uzzaman, Y. Chi, J.B.P. Lim, Web crippling capacity of fastened cold-formed steel channels with edge-stiffened web holes, un-stiffened web holes and plain webs under two-flange loading, Thin-Walled Struct. 163 (2021) 107666. https://doi.org/10.1016/j.tws.2021.107666.

[24] B. Chen, K. Roy, Z. Fang, A. Uzzaman, C.H. Phan, G.M. Raftery, J.B.P. Lim, Shear capacity of cold-Formed steel channels with edge-stiffened web holes, unstiffened web Holes, and plain webs, J. Struct. Eng. ASCE 148(2) (2022) 04021268. https://doi.org/10.1061/(ASCE)ST.1943-541X.0003250.

[25] E. Kanthasamy, K. Thirunavukkarasu, K. Poologanathan, P. Gatheeshgar, S. Todhunter, T. Suntharalingam, M.F.M. Ishqy, Shear behaviour of doubly symmetric rectangular hollow flange beam with circular edge-stiffened openings, Eng. Struct. 250 (2022) 113366. https://doi.org/10.1016/j.engstruct.2021.113366.

[26] P. Gatheeshgar, H. Alsanat, K. Poologanathan, S. Gunalan, N. Degtyareva, I. Hajirasouliha, Web crippling behaviour of slotted perforated cold-formed steel channels: IOF load case, J. Constr. Steel Res. 188 (2022) 106974. https://doi.org/10.1016/j.jcsr.2021.106974.

[27] A.M. Yousefi, B. Samali, I. Hajirasouliha, Y. Yu, G.C. Clifton, Unified design equations for web crippling failure of cold-formed ferritic stainless steel unlipped channel-sections

with web holes, J. Build. Eng. 45 (2022) 103685. https://doi.org/10.1016/j.jobe.2021.103685.

[28] P. Gatheeshgar, H. Alsanat, K. Poologanathan, S. Gunalan, N. Degtyareva, S. Wanniarachchi, I. Fareed, Web crippling of slotted perforated Cold-Formed Steel channels under EOF load case: Simulation and design, J. Build. Eng. 44 (2021) 103306. https://doi.org/10.1016/j.jobe.2021.103306.

[29] N. Degtyareva, K. Poologanathan, M. Mahendran, Web crippling tests of cold-formed steel channels with staggered web perforations, Thin-Walled Struct. 159 (2021) 107314. https://doi.org/10.1016/j.tws.2020.107314.

[30] J. Zhao, K. Sun, C. Yu, J. Wang, Tests and direct strength design on cold-formed steel channel beams with web holes, Eng. Struct. 184 (2019) 434-446. https://doi.org/10.1016/j.engstruct.2019.01.062.

[31] C.D. Moen, B.W. Schafer, Elastic buckling of cold-formed steel columns and beams with holes, Eng. Struct. 31(12) (2009) 2812-2824. https://doi.org/10.1016/j.engstruct.2009.07.007.

[32] C.D. Moen, A. Schudlich, and A.V.D. Heyden, Experiments on cold-formed steel C-section joists with unstiffened web holes, J. Struct. Eng. ASCE 139(5) (2013) 695-704. https://doi.org/10.1061/(ASCE)ST.1943-541X.0000652.

[33] N. Yu, B. Kim, L. Li, W. Hong, W. Yuan, Distortional buckling of perforated cold-formed steel beams subject to uniformly distributed transverse loads, Thin-Walled Struct. 148 (2020) 106569. https://doi.org/10.1016/j.tws.2019.106569.

[34] N. Yu, B. Kim, W. Yuan, L. Li, F. Yu, An analytical solution of distortional buckling resistance of cold-formed steel channel-section beams with web openings, Thin-Walled Struct. 135 (2019) 446-452. https://doi.org/10.1016/j.tws.2018.11.012.

[35] N. Degtyareva, P. Gatheeshgar, K. Poologanathan, S. Gunalan, K.D. Tsavdaridis, S. Napper, New distortional buckling design rules for slotted perforated cold-formed steel beams, J. Constr. Steel Res. 168 (2020) 106006. https://doi.org/10.1016/j.jcsr.2020.106006.

[36] N. Degtyareva, P. Gatheeshgar, K. Poologanathan, S. Gunalan, I. Shyha, A. McIntosh, Local buckling strength and design of cold-formed steel beams with slotted perforations, Thin-Walled Struct. 156 (2020) 106951. https://doi.org/10.1016/j.tws.2020.106951.

[37] C.H. Pham, Shear buckling of plates and thin-walled channel sections with holes, J. Constr. Steel Res. 128 (2017) 800-811. https://doi.org/10.1016/j.jcsr.2016.10.013.

[38] M.F.M. Ishqy, S. Wanniarachchi, K. Poologanathan, S. Gunalan, P. Gatheeshgar, T. Suntharalingam, S. Navaratnam, Shear behaviour of cold-formed stainless-steel beams with web openings: Numerical studies, Struct. 31 (2021) 127-144. https://doi.org/10.1016/j.istruc.2021.01.049.

[39] C.H. Pham, G.J. Hancock, Shear tests and design of cold-formed steel channels with central square holes, Thin-Walled Struct. 149 (2020) 106650. https://doi.org/10.1016/j.tws.2020.106650.

[40] D.K. Pham, C.H. Pham, S.H. Pham, G.J. Hancock, Experimental investigation of high strength cold-formed channel sections in shear with rectangular and slotted web openings, J. Constr. Steel Res. 165 (2020) 105889. https://doi.org/10.1016/j.jcsr.2019.105889.

[41] D.K. Pham, C.H. Pham, G.J. Hancock, Parametric study for shear design of cold-formed channels with elongated web openings, J. Constr. Steel Res. 172 (2020) 106222. https://doi.org/10.1016/j.jcsr.2020.106222.

[42] M.P. Kulatunga, M. Macdonald, Investigation of cold-formed steel structural members with perforations of different arrangements subjected to compression loading, Thin-Walled Struct. 67 (2013) 78-87. http://dx.doi.org/10.1016/j.tws.2013.02.014.

[43] M.P. Kulatunga, M. Macdonald, J. Rhodes, D.K. Harrison, Load capacity of cold-formed column members of lipped channel cross-section with perforations subjected to compression loading - Part I: FE simulation and test results, Thin-Walled Struct. 80 (2014) 1-12. http://dx.doi.org/10.1016/j.tws.2014.02.017.

[44] C.D. Moen, B.W. Schafer, Direct strength method for design of cold-formed steel columns with holes, J. Struct. Eng. ASCE 137(5) (2011) 559-570. https://doi.org/10.1061/(ASCE)ST.1943-541X.0000310.

[45] C.D. Moen, B.W. Schafer, Experiments on cold-formed steel columns with holes, Thin-Walled Struct. 46(10) (2008) 1164-1182. https://doi.org/10.1016/j.tws.2008.01.021.

[46] J. Rahman, K.S. Ahmed, N.I. Khan, K. Islam, S. Mangalathu, Data-driven shear strength prediction of steel fiber reinforced concrete beams using machine learning approach, Eng. Struct. 233 (2021) 111743. https://doi.org/10.1016/j.engstruct.2020.111743.

[47] M.A.B. Kabir, A.S. Hasan, A.M. Billah, Failure mode identification of column base plate connection using data-driven machine learning techniques, Eng. Struct. 240 (2021) 112389. https://doi.org/10.1016/j.engstruct.2021.112389.

[48] M. Sujith, J.S. Jeon, Machine learning-based failure mode recognition of circular reinforced concrete bridge columns: Comparative study, J. Struct. Eng. ASCE 145(10) (2019) 04019104.1-04019104.12. https://doi.org/10.1061/(ASCE)ST.1943-541X.0002402.

[49] S. Kameshwar, S. Misra, J.E. Padgett, Decision tree based bridge restoration models for extreme event performance assessment of regional road networks, Struct. Infrastruct. Eng. 16 (2020) 431-451. https://doi.org/10.1080/15732479.2019.1668026.

[50] J.S. Huang, J.X. Liew, K.M. Liew, Data-driven machine learning approach for exploring and assessing mechanical properties of carbon nanotube-reinforced cement composites, Compos. Struct. 267 (2021) 113917. https://doi.org/10.1016/j.compstruct.2021.113917.

[51] B. Keshtegar, M. Bagheri, Z.M. Yaseen, Shear strength of steel fiber-unconfined reinforced concrete beam simulation: Application of novel intelligent model, Compos. Struct. 212 (2019) 230-242. https://doi.org/10.1016/j.compstruct.2019.01.004.

[52] P. Yue, L. Zhang, Roles of artificial intelligence in construction engineering and management: A critical review and future trends, Autom. Constr. 122 (2021) 103517. https://doi.org/10.1016/j.autcon.2020.103517.

[53] S. Mangalathu, H. Jang, S.H. Hwang, J.S. Jeon, Data-driven machine-learning-based seismic failure mode identification of reinforced concrete shear walls, Eng. Struct. 208 (2020) 110331. https://doi.org/10.1016/j.engstruct.2020.110331.

[54] Z. Fang, K. Roy, Q. Ma, A. Uzzaman, J.B.P. Lim, Application of deep learning method in web crippling strength prediction of cold-formed stainless steel channel sections under end-two-flange loading, Struct. 33 (2021) 2903-2942. https://doi.org/10.1016/j.istruc.2021.05.097.

[55] Z. Fang, K. Roy, J. Mares, C.W. Sham, B. Chen, J.B.P. Lim, Deep learning-based axial capacity prediction for cold-formed steel channel sections using Deep Belief Network, Struct. 33 (2021) 2792-2802. https://doi.org/10.1016/j.tws.2021.108076.

[56] T. Chen, C. Guestrin, XGBoost: A scalable tree boosting system, the 22nd ACM SIGKDD International Conference ACM (2016).

[57] V.V. Degtyarev, K.D. Tsavdaridis, Buckling and ultimate load prediction models for perforated steel beams using machine learning algorithms, J. Build. Eng. 51 (2022) 104316. https://doi.org/10.1016/j.jobe.2022.104316.

[58] ABAQUS Analysis User's Manual-Version 6.14-2, ABAQUS Inc., USA, 2018.

[59] Z. Fang, K. Roy, H. Liang, K. Poologanathan, K. Ghosh, A.M.M. Ahmed, J.B.P. Lim, Numerical simulation and design recommendations for web crippling strength of cold-formed Steel channels with web holes under interior-one-flange loading at elevated temperatures, Buildings. 11(12) (2021) 666. https://doi.org/10.3390/buildings11120666.

[60] Z. Fang, K. Roy, Y. Chi, B. Chen, J. B.P. Lim, Finite element analysis and proposed design rules for cold-formed stainless steel channels with web holes under end-one-flange loading, Struct. 34 (2021) 2876-2899. https://doi.org/10.1016/j.istruc.2021.09.017.

[61] Z. Fang, K. Roy, A. Uzzaman, J. B.P. Lim, Numerical simulation and proposed design rules of cold-formed stainless steel channels with web holes under interior-one-flange loading, Eng. Struct. 252 (2021) 113566. https://doi.org/10.1016/j.engstruct.2021.113566.

[62] K. Roy, B.S. Chen, Z. Fang, A. Uzzaman, X. Chen, J.B.P. Lim, Local and distortional buckling behaviour of back-to-back built-up aluminium alloy channel section columns, Thin-Walled Struct. 163(1) (2021) 107713. https://doi.org/10.1016/j.tws.2021.107713.

[63] K. Roy, B. Chen, Z. Fang, A. Uzzaman, J.B.P. Lim, Axial capacity of back-to-back built-up aluminium alloy channel section columns, J. Struct. Eng. (ASCE) 148(2) (2022). https://doi.org/10.1061/(ASCE)ST.1943-541X.0003238.

[64] K. Roy, H. H. Lau, Z. Fang, A. M. M. Ahmed, J. B.P. Lim, Axial capacity of back-to-back built-up cold-formed stainless steel unlipped channels-Numerical investigation and parametric study, Steel Compos. Struct. 40(5) (2021) 761-780. https://doi.org/10.12989/scs.2021.40.5.761.

[65] Z. Fang, K. Roy, B.S. Chen, Z. Xie, J.B.P. Lim, Local and distortional buckling behavior of aluminium alloy back-to-back channels with web holes under axial compression, J. Build. Eng. 47 (2022) 103837. https://doi.org/10.1016/j.jobe.2021.103837.

[66] J. Ye, F.J. Meza, I. Hajirasouliha, J. Becque, P. Shepherd, K. Pilakoutas, Experimental investigation of cross-sectional bending capacity of cold-formed steel channels subject to local-distortional buckling interaction, J. Struct. Eng. ASCE 145(7) (2022) 04019064. https://doi.org/10.1061/(ASCE) ST.1943-541X.0002344.

[67] P. Gatheeshgarm, K. Poologanathan, S. Gunalan, B. Nagaratnam, K.D. Tsavdaridis, J. Ye, Structural behaviour of optimised cold-formed steel beams, Steel Constr. 13(4) (2020) 294-304. https://doi.org/10.1002/stco.201900024.

[68] J. Ye, S.M. Mojtabaei, I. Hajirasouliha, P. Shepherd, K. Pilakoutas, Strength and deflection behaviour of cold-formed steel back-to-back channels, Eng. Struct. 177 (2018) 641-654. https://doi.org/10.1016/j.engstruct.2018.09.064.

[69] S.J. Qadir, V.B. Nguyen, I. Hajirasouliha, B. Cartwright, M.A. English, Optimal design of cold roll formed steel channel sections under bending considering both geometry and cold work effects, Thin-Walled Struct. 157 (2020) 107020. https://doi.org/10.1016/j.tws.2020.107020.

[70] B.W. Schafer, Z. Li, C.D. Moen, Computational modeling of cold-formed steel, Thin-Walled Struct. 48 (2010) 752-762. https://doi.org/10.1016/j.tws.2010.04.008.

[71] J. Ye, I. Hajirasouliha, J. Becque, K. Pilakoutas, Development of more efficient cold-formed steel channel sections in bending, Thin-Walled Struct. 101 (2016) 1-13. https://doi.org/10.1016/j.tws.2015.12.021.

[72] J. Ye, S.M. Mojtabaei, I. Hajirasouliha, K. Pilakoutas, Efficient design of cold-formed steel bolted-moment connections for earthquake resistant frames, Thin-Walled Struct. 150 (2020) 105926. https://doi.org/10.1016/j.tws.2018.12.015.

[73] S.M. Mojtabaei, J. Ye, I. Hajirasouliha, Development of optimum cold-formed steel beams for serviceability and ultimate limit states using Big Bang-Big Crunch

optimisation, Eng. Struct. 195 (2019) 172-181. https://doi.org/10.1016/j.engstruct.2019.05.089.

Nomenclature

a	Hole diameter;
A	Ratio of the hole diameter to web depth;
b_w	Total web depth;
b_f	Total flange width;
b_l	Total lip width;
CFS	Cold-formed steel;
CFSCB	Cold-formed steel channel beam;
COV	Coefficient of variation;
DSM	Direct strength method;
E	Elastic Young's modulus;
ESH	Edge-stiffened hole;
Err	Absolute percentage error of machine learning;
FE	Finite element;
FEA	Finite element analysis;
f_y	Yield strength;
G	Elastic shear modulus;
I_y	Moment of inertial in short axis of the CFSCB;
I_{yavg}	Average moment of inertial in short axis of the CFSCB;
I_{yg}	Moment of inertial of gross section in short axis of the CFSCB;
I_{ynet}	Moment of inertial of net section in short axis of the CFSCB;
J	Torsion constant of the CFSCB;
J_{avg}	Average torsion constant of the CFSCB;
J_g	Torsion constant of gross section of the CFSCB;
J_{net}	Torsion constant of net section of the CFSCB;
L	Total length of the CFSCB;
L_{crd}	Distortional buckling half-wavelength of the gross section;

L_g	Total length of gross section of the CFSCB;
L_h	Total hole length in a distortional buckling half-wavelength;
L_{net}	Total length of net section of the CFSCB;
MAE	Mean absolute error of machine learning;
M_{bd}	Nominal moment capacity for distortional buckling;
M_{bdp}	Proposed moment capacity for distortional buckling of CFSCB with ESH;
M_{bep}	Proposed moment capacity for lateral-torsional buckling of CFSCB with ESH;
M_{bl}	Nominal moment capacity for local buckling;
M_{blp}	Proposed nominal moment capacity for local buckling of CFSCB with ESH;
M_{crd}	Elastic distortional buckling moment;
M_{cre}	Elastic lateral-torsional buckling moment;
M_{crl}	Elastic local buckling moment;
M_{TEST}	Moment capacity from tests;
M_{FEA}	Moment capacity from finite element analysis;
M_{odp}	Elastic distortional buckling moment of CFSCB with unstiffened hole;
M_{odp}	Elastic distortional buckling moment of CFSCB with plain web;
M_{oh}	Elastic lateral-torsional buckling moment of CFSCB with unstiffened hole;
M_{olh}	Elastic local buckling moment of CFS beam with unstiffened hole;
M_{olp}	Elastic local buckling moment of CFS beam with plain web;
M_{op}	Elastic lateral-torsional buckling moment of CFS beam with plain web;
MSE	Mean squared error of machine learning;
M_y	Member yield capacity of gross section;
M_{ynet}	Member yield capacity of net section;
n	Stiffened hole numbers;
P_{out}	Output dataset of machine learning;

q	Length of edge stiffener;
Q	Ratio of the length of stiffener to web depth;
R^2	Coefficient of determination of machine learning;
RMSE	Root mean square error of machine learning;
s	Hole spacing;
t	Thickness of section;
t_r	Reduced thickness of perforated section;
USH	Un-stiffened hole;
W	Web depth used in the specimen label;
Z_f	Section modulus of gross section;
Z_{fnet}	Section modulus of net section;
λ_d	Non-dimensional slenderness of distortional buckling;
λ_l	Non-dimensional slenderness of local buckling;
λ_{d1}, λ_{d2}	Limiting slenderness values;
$\sigma_{0.2}$	Static 0.2% proof stress;
σ_u	Static ultimate tensile strength;